



HAL
open science

Resonances and Lander Modes Observed by InSight on Mars (1–9 Hz)

Nikolaj Dahmen, Géraldine Zenhäusern, John Clinton, Domenico Giardini, Simon Stähler, Savas Ceylan, Constantinos Charalambous, Martin van Driel, Kenneth Hurst, Sharon Kedar, et al.

► **To cite this version:**

Nikolaj Dahmen, Géraldine Zenhäusern, John Clinton, Domenico Giardini, Simon Stähler, et al.. Resonances and Lander Modes Observed by InSight on Mars (1–9 Hz). *Bulletin of the Seismological Society of America*, 2021, 111 (6), pp.2924-2950. 10.1785/0120210056 . hal-03917215

HAL Id: hal-03917215

<https://u-paris.hal.science/hal-03917215>

Submitted on 23 Sep 2023

HAL is a multi-disciplinary open access archive for the deposit and dissemination of scientific research documents, whether they are published or not. The documents may come from teaching and research institutions in France or abroad, or from public or private research centers.

L'archive ouverte pluridisciplinaire **HAL**, est destinée au dépôt et à la diffusion de documents scientifiques de niveau recherche, publiés ou non, émanant des établissements d'enseignement et de recherche français ou étrangers, des laboratoires publics ou privés.

Resonances and Lander Modes observed by InSight on Mars (1-9 Hz)

Nikolaj L. Dahmen*, Géraldine Zenhäusern, John F. Clinton, Domenico Giardini, Simon C. Stähler, Savas Ceylan, Constantinos Charalambous, Martin van Driel, Kenneth J. Hurst, Sharon Kedar, Philippe Lognonné, Naomi Murdoch, Robert Myhill, Mark P. Panning, William T. Pike, Martin Schimmel, Cédric Schmelzbach, John-Robert Scholz, Alexander E. Stott, Eleonore Stutzmann, and William B. Banerdt

* Corresponding author: Nikolaj Dahmen, Institute of Geophysics, ETH Zurich, NO E 17, 8092 Zurich, Switzerland, +41 44 632 89 18, nikolaj.dahmen@erdw.ethz.ch

Declaration of Competing Interests

The authors acknowledge there are no conflicts of interest recorded.

Abstract

NASA's InSight lander successfully touched down on Mars in November 2018 and for the first time, a seismometer was deployed on the surface of the planet. The seismic recordings reveal diurnal and seasonal changes of the broadband noise level, which are consistent with variations of the local atmospheric conditions. The seismic data include a variety of spectral peaks, which are interpreted as wind-excited, mechanical resonances of the lander, resonances of the subsurface, or artifacts produced in the measurement system. Understanding the origin of these signals is critical for the detection and characterization of marsquakes, as well as for studies investigating the ambient noise. We identify the major spectral peaks up to 9 Hz, corresponding to the frequency range most relevant to observed marsquakes. We track the variations in frequency, amplitude and polarization of these peaks over the duration of the mission so far. The majority of these peaks can readily be classified as measurement artifacts or lander resonances (lander modes), of which the latter have a temperature-dependent peak

22 frequency and a wind-sensitive amplitude. Of particular interest is a prominent resonance at
23 2.4 Hz, which is used to discriminate between seismic events and local noise, and is possibly
24 produced by a subsurface structure. In contrast to the lander modes, the 2.4 Hz resonance
25 has distinctly different features: 1) a broad and stable spectral shape, slightly shifted on each
26 component; 2) predominantly vertical energy/polarization; 3) temperature-independent peak
27 frequency; 4) comparatively weak amplification by local winds, though there is a slow change
28 in the diurnal and seasonal amplitude; 5) excitation during all seismic events that excite this
29 frequency band. Based on these observations, we suggest that the 2.4 Hz resonance is the only
30 mode below 9 Hz that could be related to a local ground structure.

31 **Introduction**

32 The NASA InSight lander has been recording the seismicity of Mars since January 2019, following
33 the successful landing on November 26, 2018, in Elysium Planitia. The mission was designed to
34 investigate the interior structure, composition and dynamics of the planet (Banerdt et al., 2020;
35 Giardini et al., 2020; Johnson et al., 2020; Lognonné et al., 2020). Part of the payload is the Seis-
36 mic Experiment for Interior Structure (SEIS) package, consisting of a three-axis Very Broadband
37 (VBB) seismometer and a co-located three-axis Short Period (SP) sensor. SEIS was placed on the
38 Martian surface next to the lander, and includes a number of measures to minimize environmental
39 noise. Despite these efforts and similar to situations on Earth where seismometers record rever-
40 berations of nearby objects in contact with the surface, e.g., wind-excited oscillations of trees or
41 buildings (Johnson et al., 2019), SEIS is recording eigenmodes as well as transient signals from
42 the InSight lander and/or its subsystems (Ceylan et al., 2021). This phenomena was anticipated
43 pre-mission (Mimoun et al., 2017; Murdoch et al., 2018, 2017) and was also observed before on
44 the Moon during the Apollo missions (Latham et al., 1970a,b), and on Mars during the Viking
45 mission (Anderson et al., 1977; Lognonné and Mosser, 1993; Panning et al., 2020). Wind-excited
46 mechanical resonances or thermal adjustments on the lander produce long term resonances and
47 transient signals respectively. These signals have been a first-order feature of InSight’s seismic
48 dataset. Understanding them is of vital importance for studies of ambient noise recordings, as in
49 approaches such as autocorrelation (Compaire et al., 2021; Schimmel et al., 2021), where they
50 could be inadvertently interpreted as ground structure. Also, the distribution of seismic energy in

51 certain frequency bands aids in detecting and interpreting seismic events, as is routinely done by
52 the Marsquake Service (MQS, [Clinton et al. \(2018\)](#)).

53 In this study, we aim to characterize all spectral peaks that are present in the continuous 10
54 and 20 samples per second (sps) data streams, which include the frequency range most relevant to
55 marsquakes. We show that many spectral peaks are associated with wind-excited vibrations of the
56 lander system, including any component of InSight, the SEIS setup, or other instrument. We refer
57 to these as *lander modes* and though this connection is only demonstrated later in the manuscript,
58 for readability, we adopt this terminology from the here on.

59 Seismic events with energy above 2 Hz commonly excite a broad resonance at 2.4 Hz, which
60 appears to be decoupled from local noise disturbances. Seismic events do not excite any other
61 resonance. Consequently, the energy changes at 2.4Hz are used to discriminate seismic event
62 energy from local noise perturbations ([Clinton et al., 2021](#)). This 2.4 Hz resonance has been
63 interpreted as a local subsurface structure ([Clinton et al., 2021](#); [van Driel et al., 2021](#)); however,
64 its mechanism is not fully understood yet. Geological studies ([Golombek et al., 2020a,b](#); [Pan et al.,](#)
65 [2020](#)) of the landing site indicate that low-velocity layers could be present in the subsurface, which
66 could generate ground resonances.

67 Motivated by these observations, we analyze the 2.4 Hz resonance in detail and present its dis-
68 tinctly different features compared to the lander modes. It is important to note that this paper
69 remains descriptive and does not go into modeling either a subsurface resonance or specific lander
70 eigenmodes. This requires studies on its own, for instance, following the pre-mission lander eval-
71 uation by [Mimoun et al. \(2017\)](#) and [Murdoch et al. \(2018\)](#). Apart from resonating frequencies at
72 2.4 Hz and others attributed to the lander, a third type of spectral peak clearly visible in the data
73 is produced as an artifact in the measurement system (termed tick noise). An initial qualitative
74 description of these three types is given in [Ceylan et al. \(2021\)](#).

75 In this manuscript we present the available datasets of seismic and atmospheric measurements,
76 identifying the most relevant spectral peaks up to 10 Hz, and comparing the VBB and SP seis-
77 mometers. Then, we analyse the polarization of the spectral peaks and their variation with different
78 wind and temperature conditions. We present two approaches to track the daily and seasonal vari-
79 ations of the spectral peaks in terms of spectral amplitude and peak frequency over the available
80 continuous 20 sps dataset. We focus on data recorded between Sols 182–650, where a sol indicates

81 a Martian day counted from the landing and is equivalent to ~ 24 h 40 min on Earth. Finally, we
82 present the distinct features of the 2.4 Hz resonance and discuss its possible origin.

83 **Instruments, data, and observed spectral peaks**

84 **Lander location and payload**

85 The lander is located at 4.502° North and 135.623° East, just north of the dichotomy boundary
86 separating the northern lowlands from the southern highlands. Western Elysium Planitia, where
87 InSight is located, is a volcanic plain dating from the Hesperian (3.8 – 3.0 Ga) to Amazonian (<
88 3 Ga) (Banerdt et al., 2020; Golombek et al., 2020b). At the local scale, InSight landed within the
89 informally named Homestead Hollow, a roughly 25 m diameter circular depression that is inter-
90 preted as a sediment-filled, degraded impact crater (Golombek et al., 2020b). The sediments are
91 approximately 3–5 m deep and overlay Hesperian–Early Amazonian basaltic lava flows (Banerdt
92 et al., 2020; Golombek et al., 2020c).

93 After the successful landing, InSight’s robotic arm, the Instrument Deployment Arm (IDA),
94 placed SEIS on the Martian surface as far away from the lander as possible (~ 1.8 m). The sen-
95 sors remain connected to the lander by a tether, which includes an extra loop for the mechanical-
96 decoupling of the connection which is termed the Load Shunt Assembly (LSA). SEIS was then
97 covered by the Wind and Thermal Shield (WTS) that reduces environmental effects on the seismic
98 recordings. Measurements of surface pressure, wind, and temperature by the Auxiliary Payload
99 Sensor Suite (APSS) and its subsystem Temperature and Winds for InSight (TWINS, Banfield
100 et al. (2018, 2020); Spiga et al. (2018)) aid in characterizing the remaining atmospherically in-
101 duced seismic noise (Charalambous et al., 2021). Another important experiment is the Heat Flow
102 and Physical Properties Package (HP³), which was also placed on the surface next to the lander.
103 HP³ consists of the instrument housing and a 40 cm long heat flow probe that was expected (but
104 failed) to self-dig between 3–5 m into the Martian soil (Banerdt et al., 2020; Spohn et al., 2018).
105 The workspace is described in detail in Lognonné et al. (2019) and is sketched in Figure 1 of
106 Ceylan et al. (2021).

107 **Seismic, wind, and temperature measurements**

108 We analyze the spectral peaks in the seismic data recorded by the VBB and SP seismometers,
109 and compare them to the TWINS wind and atmospheric temperature measurements (see Data and
110 Resources). In Figure 1, we present the available data taking the example of Sol 319, which
111 has representative conditions for the summer in the northern hemisphere. Shown are the TWINS
112 horizontal wind speed (Fig. 1 (a)), the atmospheric temperature measured on the lander deck
113 and the scientific temperature recorded inside the VBB and SP sensor assembly (Fig. 1 (b)),
114 the spectrogram of the 100 sps SP vertical component between 9–50 Hz (Fig. 1 (c)), and the
115 spectrograms of the three 20 sps VBB components (Fig. 1 (d)-(e)). The seismic data are corrected
116 for the instrument response, including a pre-filter (VBB 30 s to 9 Hz, SP 30 s to 47 Hz), and the
117 components are rotated from the oblique orientation to the geographic coordinate system (vertical
118 (Z) / north (N) / east (E)). For that purpose, we use the openly-available SEIS station metadata (see
119 Data and Resources, which incorporate the orientation of the instrument found by [Savoie et al.](#)
120 [\(2021\)](#)). On all seismic streams, we observe a diurnal division of the seismic noise level into three
121 broad regimes, which appears to be strongly influenced by the local weather and is matched by
122 the wind speed measurements. The noise level is at its minimum during the evening, increases
123 during the night due to moderate winds, and reaches its maximum during the daytime owing to
124 strong winds and atmospheric turbulence. In addition to an increase of the broadband noise level
125 in windy periods, spectral peaks appear at distinct frequencies (e.g., ~ 4 Hz, 7 Hz). These peaks are
126 usually strongest on the horizontal components and some of them show a clear correlation between
127 frequency and temperature.

128 In contrast to these narrowband peaks is a much broader resonance around 2.4 Hz, which is
129 strongest on the vertical component and is clearly seen in the quiet evening period (it can also
130 be identified during low noise windows in the night and daytime). Unlike the narrowband peaks,
131 the 2.4 Hz resonance is excited by many marsquakes as cataloged by MQS ([Clinton et al. \(2021\)](#)),
132 see Data and Resources). Two events with energy around the 2.4 Hz resonance were detected on
133 Sol 319, namely S0319a at 03:40 Local Mean Solar Time (LMST) and S0319b at 17:35 LMST
134 ([Clinton et al., 2021](#)). A third type of persistent signal, a very narrow spectral peak seen here in the
135 East component at 1 Hz or in the North component at 2 Hz. This relates to the tick noise, which
136 is an artifact produced by cross-talk in the measurement system. The signal is constant in spectral

137 amplitude (given in velocity, $m^2/s^2/Hz$, throughout this manuscript) and frequency, and is visible
138 across the data, including harmonic overtones at higher frequencies. The tick noise is described
139 in [Ceylan et al. \(2021\)](#), and in more detail along with a procedure for its removal in [Zweifel et al.](#)
140 [\(2021\)](#).

141 The frequency content above 10 Hz (Fig. 1 (c)) features additional spectral peaks which are often
142 overlapping as they wander across the sol. Among them are several peaks around 10–12 Hz that
143 shift to lower frequencies during the daytime and are consequently appearing only then in the
144 VBB 20 sps data. Another group of peaks with particular high amplitudes are found around 25 Hz,
145 which might be partly related to the LSA (all three SP components with the full frequency range
146 are given in the Supplemental Material, Fig. S1).

147 Other outstanding features that are regularly observed in the data set are transient pulses that
148 appear 1) at frequencies below 1 Hz with 25–30 s duration, called glitches. The current under-
149 standing is that they are caused by SEIS-internal stress relaxations or by tilts of the instrument;
150 they are described in detail in [Scholz et al. \(2020\)](#). Other transient pulse are visible 2) at high
151 frequencies above 10 Hz with few seconds duration, called donks; 3) combinations of both types
152 (e.g., VBB: Sol 319 at \sim 20:40 LMST). The observed donks occur most frequently across sunset
153 (SP: Sol 319, 17–18 LMST) and involve strong transient excitation of modes above 10 Hz. An
154 overview of these and other features from non-seismic sources (e.g. the signal on the vertical SP
155 channel between 2–6 LMST, which shifts from 50 Hz down to 30 Hz, termed whistling) is given
156 in [Ceylan et al. \(2021\)](#).

157 The atmospheric temperature, wind speed, and wind direction are measured by the two TWINS
158 booms, which are mounted on top of the lander at a height of \sim 1.2 m above the Martian surface and
159 are facing outward over InSight's solar panels in opposite directions ([Banfield et al., 2018, 2020](#)).
160 To retrieve a more reliable estimate of the atmospheric conditions, both sensors are combined in a
161 composite channel that incorporates the predominant wind direction and corrects for the influence
162 of the lander ([Banfield et al., 2020](#)). The wind measurements have an accuracy of \pm 1 m/s for
163 speed, and \pm 22.5° for direction, but both speed and direction recordings are limited by a lower
164 reliability threshold for wind speeds below 1.8–2.8 m/s (derived from Reynolds number of 50–
165 90 for the atmospheric conditions at InSight's location, [Banfield et al. \(2020\)](#)). Values under this
166 threshold are typically found during the quiet evening period, as shown in Figure 1 for Sol 319. The

167 temperature sensors have an accuracy of ± 5 Kelvin (K), but are affected by their proximity to the
168 lander and its solar panels, and the sensor's non-negligible radiative cross-section (Banfield et al.,
169 2020). On Sol 319 (Fig. 1), the wind speed reaches values up to 23 m/s, and the temperature varies
170 from 171 to 254 K (both composite channels). The two temperature sensors display a difference of
171 up to ~ 25 K during the daytime, with higher values measured at sensor 1 in the morning (facing
172 sunrise), and conversely for sensor 2 in the afternoon (facing sunset; see Supplemental Material,
173 Fig. S2 (e)). The temperature inside the VBB and SP sensor assembly ranges from 222 to 247 K,
174 and tracks the thermal signal with a delay due to the insulating properties of the WTS and an
175 additional thermal barrier, which have a combined thermal time constant of ~ 7 h. Note that the
176 VBB instruments are inside an evacuated metal sphere with an additional 3 h thermal time constant
177 (Lognonné et al., 2019; Mimoun et al., 2017).

178 The atmospheric conditions described here are representative for the seasons spring to fall on
179 the northern hemisphere (Sol ~ 100 –500). From mid-fall and during winter (Sol 500–650 and
180 continuing), strong winds are recorded throughout the sol, leading to persistently high noise levels
181 (an overview of the atmospheric conditions is given in the Supplemental Material, for temperature
182 in Fig. S2 and wind in Figs. S3 and S4).

183 The measurements and the sampling rates of the individual instruments vary over the course
184 of the mission, and are limited by the available bandwidth for data transmission to Earth and the
185 spacecraft's available power. An overview of the existing data channels is given in Supplemental
186 Material, Figure 1 of Ceylan et al. (2021). Here we use the 10 sps (until Sol 182), 20 sps (after
187 Sol 182) and 100 sps (requested for selected periods) channels from the VBB and SP instruments,
188 the wind and temperature measurements of the atmosphere, and the temperature inside the sensor
189 assembly, which are mainly sampled at 0.1–1 sps (see Data and Resources).

190 **Identification of major spectral peaks**

191 Next, we seek to identify all relevant spectral peaks that are present in the 20 sps VBB dataset up
192 to the onset of the anti-alias filter near 9 Hz. The resonances are often only faintly visible when
193 computing the spectrum over short time windows. Therefore, we show velocity spectra for the
194 three components in Figure 2, estimated following Welch's method from 5 h records on multi-
195 ple sols using 120 s time windows. The nights from Sol 183–192, 0–5 LMST are selected, since

196 most of the modes are visible during these times and vary only slightly in peak frequency (due to
197 the relatively constant temperatures). Spectral peaks that are typically above 9 Hz, which shift to
198 lower frequencies during the daytime (see N/E component in Fig. 1), are not present. We identify
199 a variety of spectral peaks associated with: 1) predominantly horizontal and wind-excited modes
200 at 1.6 Hz, 2.7 Hz, 3.3 Hz, 3.7 Hz, 4.1 Hz, 4.2 Hz, 5.1 Hz, 5.2 Hz, 6.8 Hz, 7.8 Hz and 8.6 Hz, which
201 we will show can be attributed to the lander system; 2) a resonance at 2.4 Hz with mainly vertical
202 energy; and 3) the tick noise at 1 Hz and its multiples. In this study, we name the spectral peaks
203 by their peak frequency as observed in this figure from the early morning period. Specifically,
204 the lander modes at 1.6 Hz, 3.3 Hz, 4.1 Hz, 6.8 Hz and 8.6 Hz are clearly and consistently seen
205 over the period studied, whereas some other modes (e.g., 2.7 Hz, 3.7 Hz, 4.2 Hz, 5.1 Hz, 5.2 Hz,
206 7.9 Hz) are only observed during certain limited time periods. The latter group appears to be re-
207 lated to operational activities of the lander, or more precisely, to the changing position of InSight's
208 robotic arm. The lander modes generally feature the highest (spectral) amplitudes on the horizon-
209 tal components. The 4.1 Hz represent a special case, since it is relatively strong on the vertical
210 and hardly visible on the north component (but overall still strongest on the east component). In
211 contrast to the lander modes, the 2.4 Hz resonance is dominant on the vertical component, and has
212 lower amplitudes and slightly shifted peaks on the horizontal components. This resonance is best
213 observed in the quieter periods and will be analyzed in detail later on. The amplitude of the tick
214 noise is not related to the geographical coordinates, but depends on the position of the seismometer
215 axes (UVW) in the sensor assembly. The signal is strongest on the VBB V component ([Zweifel
216 et al., 2021](#)).

217 **Modes observed on deck**

218 Within the first three weeks after landing and prior to the deployment of SEIS on ground, the SP
219 seismometer recorded about 48 h of data on deck of the lander ([Panning et al., 2020](#)). From this pe-
220 riod, we select the evening of Sol 20 and show the velocity spectra computed around $\sim 21:00$ LMST
221 in Figure 3. The broadband noise level and the visible spectral peaks are several orders of mag-
222 nitude higher compared to the recordings on the ground due to the sensor's location on the wind-
223 excited lander and the absence of the WTS. We mark the expected frequency range of the previ-
224 ously identified 1.6 Hz, 3.3 Hz, 4.1 Hz, 6.8 Hz and 8.6 Hz lander modes, which are, as we will

225 show later, temperature-dependent and vary throughout the day. We find spectral peaks at each of
226 the marked frequencies. The observation of these peaks before the deployment of the seismome-
227 ters and other instruments on ground (and the opening of the LSA), points to a lander origin. We
228 see additional spectral peaks at 5.9 Hz and 7.7 Hz (up to the 9 Hz cut-off filter), which are only
229 observed on deck and could result from the specific position of the instruments and the robotic arm
230 during this period. Similar temporary modes are covered in the next section.

231 **Temporary lander modes**

232 It is common to observe spectral peaks that only appear during limited periods of the mission. The
233 frequency and spectral amplitude of these peaks vary, which makes it difficult to catalog them,
234 since some were only visible for hours on single sols. The Instrument Deployment Arm is a likely
235 source for many of these temporary modes, as it acts as a cantilever with varying geometry - its
236 position has changed dramatically over the course of the mission so far. The arm has a five-finger
237 grapple and scoop attached and its primary purpose was the deployment of both SEIS and HP³ on
238 the surface of Mars. A brief overview of main occupations for the arm follows, as we show each
239 of these occupations is associated with particular transient modes. The IDA was mainly occupied
240 with HP³-related activities during the bulk of the period analyzed in this manuscript. HP³ was
241 moved from the lander deck onto the ground on Sol 76 and its heat flow probe (mole) started
242 hammering activity in the following sols. However, it failed to penetrate the Martian regolith as
243 intended and thus the IDA was used to investigate the issue. On Sol 189, the IDA grabbed the HP³
244 housing with the grapple. The housing was then subsequently lifted off the ground and moved
245 closer to the lander, exposing the mole on the surface. The grapple was then secured on the IDA
246 and the IDA continued to inspect and interact with the mole. Between Sol 240 and 257, the scoop
247 was used to dig into the soil close to the mole to investigate soil properties. In preparation for the
248 solar conjunction (when Mars is on the opposite side of the Sun to the Earth) and resulting loss
249 of connection to InSight from Sol 267 to 288, the IDA was secured in a parking position close
250 to the western lander leg. After Sol 300, the IDA aided the mole in digging into the Martian soil
251 by pinning the mole with the scoop. Occasionally, the IDA was moved away to assess the state
252 of the mole. Each of these 'occupations' of the robotic arm coincides with different temporary
253 modes. Figure 4 shows the temporary modes, IDA position, and associated arm occupation for

254 Sols 75–650. The position is given in the IDA reference frame, where the origin is at the base of
255 the IDA which is fixed on the lander deck. $+x$ is towards the workspace, away from the lander.
256 $-x$ describes positions above the deck of the lander. $+y$ are positions towards SEIS (right side
257 when looking out from the lander), $-y$ are positions in direction of HP³. $+z$ are positions below
258 the level of the lander deck. The surface of Mars is at 1.05 m on the z -coordinate. $-z$ are positions
259 above the level of the lander deck. th describes the orientation of the tool at the end of the IDA. For
260 more detail on the IDA and the coordinate frames see [Trobi-Ollenu et al. \(2018\)](#). The background
261 shading in Figure 4 represents the general IDA occupation at a given time. They are summarized
262 in Table 1.

263 For each sol, the appearance of transient modes and the associated frequency at the start of each
264 sol are manually identified. The frequency is determined by eye and subject to some uncertainty.
265 The general absence of modes above 5 Hz before Sol 182 should be interpreted with caution, as the
266 continuous data stream is at 10 sps and 20 sps are only partly available. The majority of temporary
267 modes are seen when the grapple was out (2) and grabbed (1) and lifted HP³ (5). On Sols 205
268 and 206, when the HP³ housing was suspended from the IDA, 8 temporary modes between 1 and
269 8 Hz are seen. In contrast, pinning the mole resulted in very few, if any, temporary modes. Two
270 modes may be related to the HP³ tether and the hammering. The first appears after the deployment
271 of HP³ slightly above 4 Hz, and has a decreasing frequency over the subsequent sols. It assumes
272 a more stable frequency at around 3.8 Hz after Sol 92, where extensive mole hammering resulted
273 in the mole reaching a depth of about 30 cm, and the HP³ housing was shifted by about 2 cm. At
274 this time, the mole was coupling the HP³ housing to the ground. The second mode appears in the
275 afternoon of Sol 92 at a frequency of 2.8 Hz. Since this mode is only observed while the mole
276 was coupled to the ground, we suggest this mode is caused by vibrations of the HP³ housing. Both
277 are visible until Sol 203, which is when the HP³ housing was lifted into the air and eventually
278 moved back towards the lander, reducing tension in the HP³ tether and decoupling the housing
279 from the mole. In general though, the appearance and disappearance of the majority of temporary
280 modes coincides well with changes in IDA position. The parking position that the IDA assumed
281 around the solar conjunction produced especially strong modes at 6.2 and 7.8 Hz. In addition to
282 the temporary modes that are associated to different static poses, the dynamic arm motion itself
283 can also excite additional modes ([Stott et al., 2020](#)).

284 **Comparison of VBB and SP seismometers**

285 We compare the noise observed on each sensor during two different periods on Sol 422, a rare
286 occasion where 100 sps data are available from both instruments, allowing us to compare sensors
287 over the fullest possible frequency range. Figure 5 displays velocity spectra computed in periods
288 with moderate (night, 3:30–5:30 LMST) and low noise conditions (evening, 20:30–22:30 LMST).
289 During the windier period in the night, the previously described clear and persistent modes at
290 1.6 Hz, 3.3 Hz, 4.1 Hz, 6.8 Hz and 8.6 Hz are observed again. Additionally, there are many
291 overlapping peaks above 10 Hz, from which two major groups of peaks at 10–12 Hz and 25–26 Hz
292 stand out. When the recorded signal has higher (spectral) amplitudes during the night period,
293 both sensors match relatively well up to 10 Hz. Above that, although the shape of the peaks
294 continue to match very well, the sensors deviate in terms of amplitude. This is most significant
295 on the vertical component and much larger than 3 dB in relative difference, which corresponds
296 to the SEIS sensor calibration requirement. Possible reasons for these large relative differences
297 are the transfer function of SEIS on the low rigidity regolith (Lognonné et al., 2020) and the high
298 frequency interaction of the LSA with the SEIS sensor assembly. At the highest frequencies, the
299 different physical location of the sensors on the SEIS Leveling System (LVL, Lognonné et al.
300 (2019)) becomes significant. The SP sensors are each about 10 cm away from the center of mass
301 of SEIS - in contrast to the VBB sensors all placed within 5 cm of the center of mass. Hence the
302 SP sensor is more sensitive to rotations. (Fayon et al., 2018).

303 During the evening low-noise period, the spectra show significant deviations with a cross-over
304 point at 6 Hz. For frequencies below 6 Hz, the VBB records noticeably lower amplitudes than
305 the SP sensor, whereas above and up to 14 Hz, the opposite appears to be the case. As a result,
306 the peaks at 2.4 Hz and 11 Hz on the vertical component are more distinct on the VBB and SP
307 recordings respectively (see the enlargement in Fig. 5 (b)). The reason for this is that the SP is
308 recording instrument noise during quiet periods at frequencies below 6 Hz. Similarly, we interpret
309 the spectra between 6 Hz to 14 Hz during the low-noise periods as the noise floor of the VBB.
310 This interpretation is consistent with the pre-mission instrument performance evaluations (compare
311 Lognonné et al. (2019), Fig. 5 and 6). It is important to note that even for the vertical component,
312 where the difference between SP and VBB is most acute between 6 and 14 Hz during the quietest
313 times of day, the apparent VBB sensor noise is only marginally above the signal recorded by the SP.

314 Further, for all other periods of the day, even during light winds, the signal amplitude is well above
315 this apparent VBB noise floor. Hence, we use the VBB data to study the 2.4 Hz resonance and the
316 lander modes up to 9 Hz. Due to the VBB's significantly higher sensitivity at lower frequencies, it
317 is routinely preferred over the co-located SP instrument when detecting and analyzing marsquakes
318 or investigating ambient noise.

319 **Characteristics of spectral peaks**

320 **Variations with temperature and wind**

321 The daily spectrogram (Fig. 1) shows there are clear diurnal frequency variations for the lander
322 modes. To analyze a possible temperature dependence, we compute the velocity spectra (120 s win-
323 dow length) and average the spectra in groups of similar atmospheric temperatures (using TWINS
324 temperature sensor 2). We focus on the seasons of the Martian northern spring and summer with
325 available 20 sps data, corresponding to Sols \sim 182–500. This period is sectioned into 6 min long
326 segments for which we collect the spectra and sort them according to their average temperature (in
327 bins of 5 K). Figure 6 presents the results for a randomly chosen subset, with each line correspond-
328 ing to 130 h of averaged data with comparable temperatures. Since the temperature is strongly
329 correlated with the time of day and also correlates with wind speed (Fig. 1 (a), (b), and Supple-
330 mental Material, Figs. S2 and S3), the broadband noise level and the (spectral) amplitude of the
331 lander modes are lowest for values between 185–195 K (evening), they are slightly increased be-
332 tween 175–185 K (night), and highest above 210 K (daytime). We identify the major lander modes
333 at 1.6 Hz, 3.3 Hz, 4.1 Hz and 6.8 Hz, which are, however, smeared due to the averaging process.
334 The other visible peaks above 7 Hz cannot be assigned unambiguously. The peak frequencies of
335 the lander modes demonstrate a strong correlation with the temperature measurements. Taking the
336 6.8 Hz mode on the east component as an example: the peak frequency shifts from 6.8 Hz during
337 the coldest time to 5.9 Hz during the hottest time of the day. For the typical temperatures measured
338 during the calm parts of the evening (185–195 K), the mode nearly disappears. This is due to the
339 correlation of wind speed and temperature.

340 This analysis is complicated by the previously mentioned limitations of the temperature sensors.
341 Additionally, the actual temperature of different components on the lander are likely differing from

342 the atmospheric temperatures during the heating and cooling phases (in particular due to variations
343 in solar radiation), leading to a further broadening of the frequency peaks. Despite these chal-
344 lenges, we can observe diurnal frequency shifts in the order of 0.1 Hz (1.6 Hz), 0.3 Hz (3.3 Hz),
345 0.2–0.3 Hz (4.1 Hz) and 0.9 Hz (6.8 Hz) on the east component. When visible, the tick noise and
346 the 2.4 Hz resonance do not indicate any temperature dependence. These relations will be explored
347 in detail in following sections.

348 **Polarization analysis**

349 If the spectral peaks analyzed so far originate from different sources, we would expect them to
350 show different motion patterns which are visible in the seismic signal as three-dimensional particle
351 motion. In the specific case of lander modes, the seismometer is located in a distance of 1.8–
352 3.6 m from the lander feet and so is in the near-field of the source. Therefore, the recorded motion
353 is quasi-static, rather than wave-like. The polarization recorded by SEIS will be similar but not
354 identical to the source polarization, as vertical and transverse motion at the source will induce
355 a component of radial motion at SEIS (Myhill et al., 2018). Each discrete structural mode will
356 have a pattern of motion, or modeshape, resulting in an individual excitation pattern at the lander
357 feet. We use a polarization analysis following Samson (1980, 1983) and Schimmel and Gallart
358 (2003) that provides polarization ellipses parameters and the degree of polarization (*dop*). Figure
359 7 displays the scalogram, the ellipticity, the major azimuth and the major inclination, again for the
360 VBB sensor on Sol 319 (same plot for the SP sensor in in the Supplemental Material, Fig. S5). The
361 scalogram shows the length of the polarization vector, representing the total energy in the three-
362 component data for each individual time-frequency bin (120 s · 0.05 Hz bins). In the other parts
363 of Figure 7 (b)-(d), unpolarized signals are removed by using a *dop* filter (Schimmel and Gallart,
364 2004) with a window length of 120 seconds (the computed *dop* values and the same data without
365 the *dop* filter are shown in the Supplemental Material, Fig. S6). Among the remaining signals, we
366 observe the strongly polarized frequency range below 1 Hz (treated in Stutzmann et al. (2021)),
367 transient broadband pulses, and the three types of spectral peaks (lander, 2.4 Hz, tick noise).
368 The lander modes are predominantly horizontally polarized, as indicated by the low inclination
369 values. Only the 4.1 Hz mode reaches values up to $\sim 30^\circ$. The azimuths are varying from mode to
370 mode, but are confined to the range between $240\text{--}330^\circ$. Both azimuth and inclination values appear

371 to wander along with the frequency shifts during the day (a zoom-in on the values relevant for the
372 lander modes is given in Supplemental Material, Fig. S7). During the warming of the atmosphere
373 and lander, the inclination increases while the azimuth decreases (e.g., 6.8 Hz mode: inclination
374 $\sim 5^\circ$ to $\sim 15^\circ$; azimuth $\sim 290^\circ$ to $\sim 240^\circ$). In contrast, we observe steady predominantly vertical
375 particle motion and azimuth values around 180° for the 2.4 Hz resonance, visible around ~ 4 LMST
376 and 17–22 LMST. These characteristics are observed throughout the mission (see Supplemental
377 Material, Figs. S8 and S9). In general, the polarization attributes for the different resonant modes
378 are stable, independent of the method chosen. An exception though is the 2.4 Hz peak; while the
379 near-vertical inclination of the 2.4 Hz peak is well constrained, fully resolving all time-dependent
380 polarization attributes, including the azimuth, may be more dependent on the choice of algorithm
381 and parameter settings than for the lander modes.

382 **Damping of modes**

383 The structural dynamics of the lander are characterized by the damping in the system (in addition
384 to its mass and stiffness). If we assume viscous damping, the damping can be estimated from
385 the spectral shapes of the described lander modes. We use the half power bandwidth method in
386 frequency domain following Paz et al. (2019), that relates the difference or bandwidth between two
387 frequencies with the same response amplitude to the damping of the system. The bandwidth of the
388 mode is typically measured at half power of the peak amplitude, which gives the half-power points
389 or frequencies at $f_0 \pm f_w/2$ on both sides of the spectral peak, where f_0 and f_w stand for the peak's
390 frequency and width, respectively. The damping ratio ξ of the critical damping is approximated
391 by:

$$\xi = \frac{f_w}{2f_0}. \quad (1)$$

392 We calculate the half-power frequencies from the estimated center frequency and spectral width
393 of a Lorentz function that is fitted to each mode. The Lorentz function L is given by:

$$L(f) = \frac{1}{1 + w^2} \quad (2)$$

394 with

$$w = \frac{f - f_0}{f_w/2}, \quad (3)$$

395 where f is the frequency. We apply this technique to determine an equivalent viscous damping
 396 estimate for all main modes (we do not analyze the tick noise). The damping ratios are evaluated
 397 on Sol 319 for periods in the morning with moderate winds (04:30-05:00 LMST) and evening with
 398 low winds (19:30-20:00 LMST; see Fig. 1, both periods indicate relatively stable peak frequencies
 399 over the 30 min period), using the combined three-component scalogram data. For the main lan-
 400 der modes and the 2.4 Hz resonance we obtain damping ratios (morning/evening) of 1.27/1.32%
 401 (1.6 Hz), -/4.22% (2.4 Hz), 0.69/0.64% (3.3 Hz), 0.86/ 0.98% (4.1 Hz), 0.53/0.49% (6.8 Hz), and
 402 0.64/-% (8.6 Hz). The 2.4 Hz is only observed in the night, and vice versa the 8.6 Hz mode only
 403 in the morning (see Supplemental Material, Figs. S10 and S11). The other lander modes give
 404 comparable results in both periods. The lander modes are very lightly damped with values be-
 405 tween 0.5-1.3%. For lander modes associated with ground interaction, for example the lander feet
 406 vibrating on the ground, the estimate may include damping from both the structure and the ground
 407 interaction (Murdoch et al., 2018). The 2.4 Hz is clearly substantially broader and is characterized
 408 by a significantly higher damping ratio of about 4.2%.

409 **Diurnal and seasonal variations of spectral peaks**

410 **Spectral peak tracking methods**

411 As presented above, some resonances are clearly seen across the mission while others are weaker
 412 or even only transient. In this section, we track the permanent spectral peaks and quantify their be-
 413 havior with regards to wind and temperature. An automated tracking algorithm is deployed which
 414 uses spectral fitting on the three-component scalogram. This algorithm fits a Lorentz function to
 415 the spectral peaks. As the input, we define a narrow frequency band on the seismic data which
 416 includes the full frequency range of each mode. As the output, the algorithm retrieves the temporal
 417 evolution of peak frequency, (spectral) peak amplitude, spectral width, and azimuth of the mode.
 418 Our method is capable of tracking the three strongest lander modes (3.3 Hz, 4.1 Hz, 6.8 Hz), as
 419 well as the 2.4 Hz resonance across the mission so far. In addition, although it is not a mechanical
 420 resonance, we track the 1 Hz tick noise for validation of the method.

421 An alternative manual method is used to track weaker modes. We track two lander modes
422 (1.6 Hz and 8.6 Hz), simply by picking the frequency on the scalogram at a given time, and
423 determining the associated azimuth and peak amplitude. This method provides a more sparse
424 data overview of peak frequency, peak amplitude, and azimuth, as the manual picking is time
425 consuming. We choose sols at regular intervals with 40 sols spacing to sample the different seasons
426 on Mars.

427 **Spectral peak tracking over representative Sols**

428 Figure 8 presents both the automatically tracked modes and manually picked modes for Sol 319.
429 No single mode is always trackable throughout the sol, so there are gaps in each tracked time series.
430 The 1 Hz tick noise, the 1.6 Hz, and 2.4 Hz resonances are seen primarily during the quiet parts
431 of the sol and disappear from the data during the windier parts. The 3.3 Hz and the 8.6 Hz modes
432 appear during windier conditions but often disappear during noon and afternoon. These mid-day
433 gaps are less frequent in the later, windier parts of the mission. The 4.1 Hz and 6.8 Hz modes
434 similarly appear during windier times, but are stronger during the day and can be continuously
435 tracked from morning to early evening. This behavior persists across the mission. The 4.1 Hz and
436 6.8 Hz modes are the most dominant across the mission. They are strongly excited by wind and are
437 only absent during very quiet periods. From around Sol 500 onward, the wind is generally strong
438 throughout the entire sol without significant quiet periods. In this period the 3.3 Hz, 4.1 Hz, and
439 6.8 Hz modes are then seen continuously across the sol (see data gaps in Fig. S8).

440 The frequency shifts differ strongly between spectral peaks. While the 1 Hz tick noise shows
441 no change in frequency over time, the lander modes all exhibit a dip in frequency during the day.
442 In general, the higher frequency modes exhibit a larger variance in frequency. Figure 9 show
443 how temperature and modes vary across each sol for a number of different sols. Figure 9 (a)
444 presents the atmospheric temperature, with inverted y-axis to match changing frequencies. Figure
445 9 summarizes the frequency wander of all spectral peaks on (b) the same scale and on (c)-(h) an
446 individual scale. As can be seen in Figure 9 (b), the 1 Hz tick noise shows no change in frequency
447 apart from picking uncertainty. Similarly, the 2.4 Hz resonance shows no significant change over
448 the sols. The change in frequency on Sol 225 is due to picking errors by the tracking algorithm. In
449 contrast, each lander mode exhibits a dip in frequency during the day, starting at around 6:00 LMST

450 and lasting until about 18:00 LMST, tracking closely the changes in temperature. This decrease in
451 frequency varies from 0.2 Hz (for the 1.6 Hz mode, Fig. 9 (h)) to almost 2 Hz (for the 8.6 Hz mode,
452 Fig. 9 (c)). As the 1.6 Hz mode is rarely visible during the windy afternoon, the full frequency
453 drop is likely not quantified. The lander modes exhibit lower frequencies during the later parts of
454 the mission, at which times the landing site was subject to higher atmospheric temperatures as the
455 seasons changed.

456 It should be noted that the automatically tracked modes can include outlier peaks that are false.
457 Manual inspection show that this accounts only for a small part of the picks and should not interfere
458 with the overall interpretation of the data. Nevertheless, unusual behavior and high frequency jitter
459 in the plots should be interpreted with caution.

460 **Spectral peak tracking across the mission**

461 The frequency, amplitude and visibility in the spectrogram of the tracked natural resonance modes
462 are correlated with temperature and wind velocity. A systematic analysis of this behavior requires
463 concurrent availability of seismic, wind and temperature data. Although these data are generally
464 available, there are periods when some data sets are not available during the mission, for example
465 during the solar conjunction and after Sol 600 (see Supplemental Material, Figs. S2 and S3).
466 Figure 10 shows how the frequency and amplitude of the 5 tracked lander modes, as well as the
467 2.4 Hz resonance and the 1 Hz tick noise, vary with respect to the atmospheric temperature and
468 wind speed during the mission. Temperature sensor 1 is used here and temperature sensor 2 is given
469 in the Supplemental Material, Figure S12. The left column of Figure 10 shows the spectral shapes
470 of each mode as used by the tracking algorithm. Note that the peaks are different than in Figure 2,
471 as the tracking algorithm uses the scalogram, which gives a more complex shape than individual
472 components - this is particularly true for the 2.4 Hz resonance. The spectra for the 8.6 Hz mode
473 is cut for frequencies below 7.3 Hz to remove the influence of the 6.8 Hz mode. These spectra
474 provide an indication of the errors of the tracking algorithm - the narrow, high peaks such as 1 Hz
475 are easy to track, whereas for small, broad peaks such as 2.4 Hz, there is more scatter. The middle
476 column of Figure 10 plots peak resonance frequency against temperature. The 3.3 Hz, 4.1 Hz,
477 6.8 Hz, and 8.6 Hz modes show a clear hysteresis curve, with larger frequency drops tracking
478 increasing temperature (the passage of time is represented by anticlockwise paths on these plots).

479 The 1.6 Hz mode has the least amount of data points, as it is only visible during quiet parts of
480 the day and is tracked manually, so only a few sols are available. Still, similar to the other lander
481 modes, a hysteretic response is suggested, although the frequency decreases lag behind increases in
482 temperature (clockwise motion on these plots). For all lander modes, the highest frequency occurs
483 at the coldest part of the day, around 170 K and decreases steadily as the atmospheric temperature
484 increases. The minimum frequency occurs at the hottest time of the day, between 240–260 K.
485 In contrast, the 2.4 Hz resonance shows no such hysteresis curve nor any other clear temperature
486 dependence. The double peaks, one at 2.4 Hz and the other at slightly higher frequency, are due to
487 the fitting algorithm which fits the broad shape of the peak, which is far wider than for other modes,
488 and hence has a larger picking uncertainty. Since the peaks lie on top of a non-flat spectra (cf. Fig.
489 6), fitting the broad shape may shift the maximum of fitted peak with respect to the maximum of
490 the underlying peak. The frequency remains generally centered around 2.4 Hz for all temperatures.

491 In the right column of Figure 10, the amplitude of each resonant peak is plotted against the
492 recorded wind speed. Data recorded when wind speeds are below 2 m/s are not shown since the
493 wind speeds below this level are not reliable, as discussed previously. All lander modes exhibit
494 a positive correlation between amplitude and wind speed between 2 and 4 m/s. As wind speeds
495 further increase, the slope decreases, with the amplitude becoming constant above 8 m/s. A similar
496 behavior is seen on Earth by [Frankinet et al. \(2020\)](#), although they find different linear relationships
497 with seismic noise amplitude when wind speeds are below and above 6 m/s. They find a steeper
498 increase in noise amplitude with rising wind above 6 m/s.

499 The minimum amplitudes of the lander and 2.4 Hz resonances are around -200 dB [$m^2/s^2/Hz$],
500 which is consistent with the noise floor (see Fig. 5) as well as the lowest visible signatures of the
501 modes from Figure 6. In contrast, there is strong variation in the maximum amplitudes between
502 modes, reaching up to -140 dB for the 4.1 Hz mode, while the 3.3 Hz and 8.6 Hz mode only reach
503 -160 dB. These values are larger than what is seen in Figure 6. First, the values here are from
504 the three-component scalogram instead of single components. Second, the lines in Figure 6 are
505 averaged over 130 h while Figure 10 has each value calculated from a 10 min window. Thus rare,
506 very high amplitude wind speeds are not averaged out.

507 The automatically tracked modes at 3.3 Hz, 4.1 Hz, and 6.8 Hz are detected for wind speeds
508 up to 14 m/s. The 1.6 Hz mode is not seen during windy parts of the day, evident here as there is

509 no identification of the mode above 8 m/s. In a similar manner, the 2.4 Hz resonance is primarily
510 detected at wind speeds below 5 m/s. The manually tracked 8.6 Hz mode is visible at much higher
511 wind speeds, up to 12 m/s, though not higher. Since much higher wind speeds are rarer, the lack
512 of picks for this mode above 10 m/s may be due to the much sparser data coverage compared to
513 the automatically tracked modes. The histograms for the automatically tracked modes suggest that
514 wind speeds above 7 m/s are rare. The 2.4 Hz resonance has much lower amplitudes than the other
515 modes, predominantly between -200 dB and -190 dB. The amplitude has a far weaker dependence
516 on the wind speed compared to the lander modes. Careful analysis of these results indicate that the
517 cluster of higher amplitudes, -180 to -170 dB, at wind speeds between 3 and 4 m/s is mainly due to
518 the picking of a temporary mode around 2.5 Hz during the lifting of HP³ (see Fig. 4). The 1.6 Hz
519 mode is also only seen at low wind speeds. However, the amplitude increases by 30 dB with rising
520 winds while the 2.4 Hz amplitude changes by less than 10 dB. This plot quantifies the observation
521 from individual sols (Fig. 1) and averaged spectra (Fig. 6) that for the lander modes, the change in
522 frequency is mainly driven by the atmospheric temperature and clearly separates the influence of
523 wind speed, which is modulating the amplitude of the modes.

524 In order to better understand diurnal patterns, in Figure 11 we investigate the evolution of fre-
525 quency and peak amplitude across a single sample sol (Sol 319). Results using temperature sensor
526 2 are given in the Supplementary Material, Figure S13. In the left column of Figure 11, the
527 frequency of each mode is normalized by the respective frequency at 170 K (the minimum tem-
528 perature this sol), and the color indicates the time of the sol. At midnight LMST, the lander modes
529 have a relative frequency slightly below 1.00. The temperature decreases until around 05:00 LMST
530 when it reaches 170 K, which is when the modes have their highest frequencies. Afterwards, the
531 temperature rises while the frequencies decrease. The frequencies stabilize before the maximum
532 temperature is reached, something which was already seen in Figure 10. Afterwards, as the tem-
533 peratures drop rapidly in the afternoon, the frequencies rise again, though with a different slope to
534 the frequency decrease. The magnitude of the decrease in frequency is different for each mode,
535 ranging from around 5% (3.3 Hz mode) to 20% (8.6 Hz mode). The hysteresis curves are traversed
536 in counter-clockwise direction. One exception to this is the 1.6 Hz mode, which even despite the
537 limited data, appears to go in a clockwise direction. For roughly half of the sols, there are either
538 too few picks to see the shape of the hysteresis curve for the 1.6 Hz mode, or the pick uncertainty

539 is too large to reliably see in which direction the curve is traversed. However, the other half of the
540 sols show a retrograde direction. No sols with prograde, meaning counter-clockwise, hysteresis
541 curve have been found for the 1.6 Hz mode. Unlike the lander modes, the relative frequency of
542 the 2.4 Hz resonance does not change with temperature over time but rather stays at 1.00 apart
543 from minor algorithm picking uncertainties - similar to the 1 Hz tick noise. In the right column of
544 Figure 11, the wind is plotted on a logarithmic axis against the peak amplitude. On these double-
545 logarithmic plots, the relationship between peak amplitude and wind speed is roughly linear for all
546 lander modes. Similar to Figure 10, the 2.4 Hz resonance is only visible at low wind speeds and
547 shows only a comparatively weak increase in peak amplitude with wind.

548 In addition to the wind speed, the excitation efficiency of a given lander mode might depend on
549 the wind's direction. On Sol 319 (right column of Fig. 11) as well as during other periods, lower
550 wind speeds correspond to a wind direction of about 220° , while above a wind speed of 4 m/s,
551 the wind direction changes to 120° . Due to this correlation between wind speed and direction,
552 the effect of wind direction on lander mode excitation and therefore peak amplitude cannot be
553 disentangled.

554 **The 2.4 Hz resonance**

555 **Ambient excitation**

556 The previous analysis already indicated several key differences between the 2.4 Hz resonance and
557 the lander modes in terms of polarization and sensitivity to temperature and wind. In the following,
558 we focus on the 2.4 Hz resonance and summarize the main characteristics.

559 The automatic tracking of the 2.4 Hz resonance showed a larger spread in frequency compared
560 to the lander modes, which is likely caused by its broad spectral shape and influenced by changing
561 slopes of the broadband noise level for different wind conditions. For a more precise analysis,
562 we use the procedure described in the *Variations with temperature and wind* section to investigate
563 the relation with temperature and wind in detail. Figure 12 (a) presents the spectra stacked by
564 temperature, similar to Figure 6, but here restricted to periods with low wind speeds (<3.5 m/s).
565 This allows us to collect short low-noise periods during the daytime, when the 2.4 Hz resonance is
566 not hidden under the broadband noise. Each line represents the average (spectral) amplitude from

567 1130 time windows of 120 s duration (~ 38 h) that have similar average temperatures, selected
568 between Sol 182-650. In Figure 12 (b) we present the same data on a linear scale, and in (c)
569 we show an estimate of the mode's excess power. We define the excess power as the power of the
570 spectral peak above the broadband noise level. To that end, we subtract a linear fit of the noise level
571 between 1.8 Hz and 2.8 Hz. This procedure assumes the sources of the broadband and mode signals
572 are incoherent. As a test, Figure 12 (c) shows that the peak amplitude of the 2 Hz tick noise, which
573 is known to have constant amplitude (Zweifel et al., 2021), is correctly retrieved after subtraction of
574 the broadband noise. Whenever visible, the 2.4 Hz resonance reveals a temperature-independent
575 and broad spectral shape, with a dominant peak on the vertical (2.39 Hz and a smaller, slightly
576 offset peak at 2.33 Hz), and shifted peaks on the horizontal components (N: 2.36 and 2.48 Hz; E:
577 2.56 Hz). By contrast, the shape of the lander modes is obviously modulated by temperature (in this
578 Figure we see only the 3.3 Hz mode, which shows relatively minor temperature changes compared
579 to other modes, see Figure 6). Note that, for high temperatures, the broadband noise level is not
580 linear and after subtraction, negative amplitudes are obtained on the horizontal components.

581 Figure 12 (d)-(f) shows a similar analysis for spectra stacked by wind speed. Each bin with
582 similar average wind speeds contains between 1180 and 3500 time windows (at low and high wind
583 speeds respectively) of 6 min duration (118 h to 350 h), randomly selected between Sol 182-500.
584 Since we are averaging over large a data set, high-amplitude signals that are not wind-related are
585 also included and influence the analysis. We omit periods with very high noise levels (wind speeds
586 >9 m/s), when the 2.4 Hz resonance is obscured by the broadband noise. The spectra reveal the
587 gradual increase of the broadband noise level. The spectra are only overlapping for wind speeds
588 below ~ 2.5 m/s, where measurements are less reliable and we cannot distinguish between low
589 wind speeds. We observe again the same characteristic spectral shape of the 2.4 Hz resonance at
590 low absolute amplitudes, and note the complex fine structure (Z: individual peaks at 2.05, 2.14,
591 2.23, 2.33, 2.39, 2.46, 2.52, 2.57, 2.59, 2.62, 2.67, 2.71, 2.77 Hz). At wind speeds above 5 m/s
592 (Fig. 12 (d)) the amplitude of the 2.4 Hz peak appears to be buried in the noise. On the linear scale
593 (Fig. 12 (e)), we can identify the excess power of the 2.4 Hz amplitude also at higher wind speeds
594 as a result of the averaging process. The resonance's excess power is again estimated by removing
595 a linear fit of the broadband noise level. We observe a strong increase of the 3.3 Hz lander mode
596 with rising wind speeds, especially on the horizontal components. The 2.4 Hz resonance is clearly

597 observed on all components in calm wind conditions, but there is an increase in excess power at
598 higher wind speeds that appears to be correlated with wind speeds (when considering the vertical
599 component, zoom in Fig. 12 (f)).

600 We show this relation in more detail in Figure 13 (a), by extracting the excess power of the
601 2.4 Hz resonance and plotting it against wind speed. We find an increase of the vertical 2.4 Hz
602 excess power with rising wind speed. Although this analysis depends on the choice of the baseline,
603 the increase appears to go beyond variations of the tick noise at 2 Hz (added as reference). With
604 increasing wind speeds, the uncertainty in estimating the excess power becomes large as the ratio
605 of excess power to broadband noise becomes very small and we consequently only include values
606 up to 8-9 m/s. In addition, we show in Figure 13 (b) the wind sensitivity of the 3.3 Hz lander
607 mode and the broadband noise level, selected around 1.8 Hz and 2.8 Hz. We add a linear best fit
608 as a reference in the range with reliable wind speed and excess power estimates (3.75-7.5 m/s) to
609 compare the different behavior of the 2.4 Hz and 3.3 Hz modes. The estimated slope for the 2.4 Hz
610 resonances (Z) is 7.0×10^{-21} (after removing the increase of the broadband noise level which is:
611 1.8 Hz: 7.3×10^{-19} and 2.8 Hz: 8.2×10^{-19} , both Z). In comparison, the 3.3 Hz mode (N) has a
612 slope of 2.2×10^{-18} (1.8 Hz: 3.3×10^{-19} and 2.8 Hz: 5.9×10^{-19} , both N). All slopes are given
613 in units of $[\text{m}^2/\text{s}^2/\text{Hz}]/[\text{m/s}]$. When considering the components on which each mode is strongest,
614 the wind amplification of the 3.3 Hz mode is orders of magnitude higher than the 2.4 Hz increase
615 (factor of 300 in the range 3.75-7.5 m/s). The background seismic noise itself is increasing at a rate
616 100 times higher than that of the 2.4 Hz resonance, making this a difficult measurement to extract.
617 Additionally, this analysis likely underestimates the peak power of the lander mode, as each wind
618 speed bin includes a wider range of temperatures with different peak frequencies and consequently
619 broadens and flattens the peak. We derive the relation of 2.4 Hz resonance and the wind speed by
620 averaging over large amounts of data and it should be noted that we do not necessarily observe the
621 same relation when looking at individual sols (Supplemental Figs. S14 and S15).

622 Unlike the lander modes, the 2.4 Hz resonance does not show rapid changes in amplitude co-
623 inciding with varying environmental conditions, yet, there are amplitude changes on the diurnal
624 and seasonal scale. Figure 14 outlines the seasonal variations of the 2.4 Hz resonance, represented
625 by the 2.3-2.5 Hz frequency band of the vertical component. We show only periods when the
626 2.4 Hz peak is above the broadband noise level (selected by: difference in dB between 2.3-2.5 Hz

627 and 1.2-3 Hz band exceeds threshold of 6 dB; see Supplemental Material, Fig. S16). From early
628 spring to early fall, we see low-noise conditions from just before sunset to late in the evening, and
629 partly continuing in the night. In these periods, the 2.4 Hz resonance is clearly visible. During
630 the daytime, and from mid-fall on nearly throughout the whole day, strong winds are dominating.
631 The 2.4 Hz peak is then only occasionally observed during short wind lulls when the noise level
632 drops down. During these quiet windows, the 2.4 Hz amplitude appears sometimes lower than in
633 the evening, yet, these values are still consistent with the variations we see over the mission. The
634 amplitude of the 2.4 Hz peak is relatively high around the start of spring, it decreases towards the
635 start of the summer, after which it starts to rise again. In addition, the resonance displays daily
636 variations, e.g. in the period around Sol 100, or Sol 460. These changes follow daily or seasonal
637 changes of the broadband noise level, but seem to be amplified for the 2.4 Hz peak. Apart from
638 variations in amplitudes, the spectral shape of the 2.4 Hz resonance remains very stable over time
639 (see Supplemental Material, Figs. S17 and S18).

640 **Event excitation**

641 During the quiet evenings, many 10-30 min time windows with sustained high 2.4 Hz amplitude
642 stand out (see examples in Fig. 14). When looking in detail at these periods, they often show
643 distinct primary and secondary energy packages. A number of these time windows have been
644 classified as *high frequency* (HF) seismic events and are available in the MQS catalog (see Data
645 and Resources section).

646 We take a closer look at the excitation of 32 of the highest quality HF event and present their
647 velocity spectra in Figure 15 (a), (c) and (e). The spectra include the main S-wave energy and
648 are computed with a 30 s window length. During the events, the 2.4 Hz resonance maintains the
649 same spectral shape as seen before (Z: dominant peak at 2.4 Hz, N: double peaks at 2.35&2.5 Hz,
650 E: dominant peak at 2.6 Hz), but exceeds the usually observed amplitudes. This is illustrated in
651 Figure 15 (b), (d) and (f), which show the spectral difference (on a dB scale) of the events and the
652 pre-event noise window. This suggests that the HF events have a frequency content between ~ 0.5
653 to 5–6 Hz, which is greatly amplified around the 2.4 Hz resonance. The comparable increase of
654 ~ 11 dB (on average) around 2.4 Hz on all three components corresponds to a larger amplification
655 in absolute power on the vertical component (due to the dB-scale, Z: -197 to 186 dB, N&E: -204

656 to -193 dB; the given difference in dB corresponds to ratio on linear scale).

657 Figure 16 shows the polarization for one of the most significant teleseismic marsquakes recorded
658 so far, S0235b. It has a clear P-wave polarization corresponding to a back azimuth of 74° (Clinton
659 et al., 2021). Its energy spectrum extends from low frequencies to above 2 Hz and excites the 2.4 Hz
660 resonance. Figure 16 (a) shows the three-component scalogram computed using a continuous
661 wavelet transform with a 20 s window length. Figure 16 (b) and (c) depict the histograms for the
662 noise and signal time window marked in (a), respectively. In the bottom row, Figure 16 (d) shows
663 the azimuth for polarized signals and (e) and (f) are again the histograms for the noise and signal
664 time window. During the noise time window (middle column), the 2.4 Hz resonance is clearly
665 seen on the power spectrum with a peak at around -190 dB. The polarization is dominated by
666 an azimuth of around 180° while frequencies above and below have a more randomly distributed
667 azimuth. When considering the signal time window (right column of Fig. 16), the peak power of
668 the 2.4 Hz resonance increases to almost -180 dB. The azimuth in the 2.4 Hz resonance frequency
669 band is very similar to the noise time window, with a slight shift to around 200° . In contrast, lower
670 and higher frequencies align around 70° azimuth, the polarization of the P-wave. The azimuth
671 of the 2.4 Hz excitation is evidently little affected by the polarization of the event and remains
672 very similar to the azimuth of the ambient peak. Although, as mentioned previously, the apparent
673 azimuthal polarization of the 2.4 Hz energy does vary with different methodologies, it is clear that
674 even when the background wavefield is polarized during a strong marsquake, the 2.4 Hz energy
675 retains its more complex behavior.

676 Discussion

677 The resonances discussed in this paper have been a first order feature of the InSight seismic dataset
678 from the beginning of the mission and understanding their characteristics and mechanisms is there-
679 fore critical for the analysis of seismic events, as well as ambient noise. The latter is particularly
680 true for studies using the ambient noise, e.g. for auto-correlation methods. The behavior of the
681 spectral peaks with respect to atmospheric excitation, as summarized in Figure 10 and Table 2,
682 allows us to identify 4 main classes.

683 1. Completely stable spectral peaks. This is specifically the 1 Hz "tick noise" and its harmonic

684 overtones, which are not mechanical modes, but correspond to Fourier lines of a repeating
685 1 Hz signal. The signal does not change frequency or (spectral) amplitude over the mission
686 and is not affected by marsquakes in any way. It can be explained by cross-talk in the SEIS
687 tether (Zweifel et al., 2021).

- 688 2. Temperature- and wind-sensitive (lander) modes. As is clearly visible in daily spectrograms
689 (Fig. 1), the spectral peaks at 1.6 Hz, 3.3 Hz, 4.1 Hz, 6.8 Hz and 8.6 Hz change their fre-
690 quencies in a similar manner each sol. Comparison with TWINS air temperature data (Figs.
691 9 and 10) demonstrates each of these modes have a resonance frequency that is modulated by
692 atmospheric temperature. Comparison of mode amplitude with wind speed (Figs. 10 and 11,
693 right panels) indicates that the wind speed is driving the modal amplification, with a possible
694 sensitivity to wind direction. Each of these modes is very lightly damped. Since these modes
695 were also clearly observed while SEIS was still placed on the lander deck (Fig. 3), it can be
696 assumed that they are indeed caused by resonances of the lander itself. A model of lander
697 resonances was prepared before the mission (Murdoch et al., 2018), as part of the instrument
698 noise model (Mimoun et al., 2017). However, this model assumed that the lander body was
699 rigid with the exception of the flexible solar panels. In reality, the situation is more complex
700 because the lander legs also exhibit several degrees of freedom (Panning et al., 2020). It
701 is, therefore, unclear whether the predicted eigenmodes can be assigned to specific peaks
702 in the observed spectra. The shift to lower frequencies during the day is expected since the
703 lander parts expand and become more flexible when they are heated up. When the stiffness
704 decreases (inversely proportional to the length of the element), the mode frequency decrease
705 as well (proportional to stiffness). This matches the observations, yet, it has to be noted that
706 the value of $(\delta f/f_0)/\delta T$ for many of these modes is very high: $3.4 \cdot 10^{-3}$ for the 8.6 Hz
707 mode and $0.8 \cdot 10^{-3}$ for the 4.1 Hz mode. This is a 2 to 3 orders of magnitude larger than
708 expansion coefficients for metals ($5.5 \cdot 10^{-6}$ for titanium around 200 K). A likely explanation
709 is that the eigenmode frequency is also affected by the stress state of the lander, which can be
710 changed significantly even by small deformation. There is currently no engineering analysis
711 available that describes what the actual eigenmodes of the lander look like (e.g. whether the
712 modes correspond to a flapping of the solar panel or a rocking of the whole lander on the
713 springs in its legs). There are some time delays using the TWINS sensors 1 and 2. The time

714 delays between mode frequencies and atmospheric temperature sensor 1 (Fig. 10 and 11)
715 for all (lander) modes other than the 1.6 Hz mode are apparent, but they are much larger if
716 sensor 2 is used instead (Figs. S12 and S13). The 1.6 Hz mode shows no difference in time
717 delay between sensor 1 and 2, and has a retrograde hysteresis curve compared to the other
718 (lander) modes. Figure S2 shows the large difference between the two sensors, which can be
719 explained by their proximity to the different solar panels that reflect solar radiation towards
720 the sensors after sunrise and before sunset. Further, differences between mode resonant fre-
721 quencies and temperatures can be explained if one assumes that the lander is heated by solar
722 irradiation directly, while the thin atmosphere takes longer to warm up, similar to what is
723 observed on sunny cold mornings on Earth, where surfaces can heat up significantly while
724 the air is still cold. As no temperature sensor is installed in the metal frame of the lander, its
725 temperature curve cannot be quantified directly. Measurements of the ground temperature
726 by infrared sensor by another instrument package, the HP³, show that the ground surface
727 around the lander reacts more quickly than the atmosphere to irradiation changes either due
728 to sunrise and sunset (Mueller et al., 2020), or on shorter time scales, eclipses of the Martian
729 moon Phobos (Stähler et al., 2020). Since the ground temperature is not measured contin-
730 uously, it cannot be compared directly to the lander mode frequencies. Another important
731 observation is that these modes have not been excited by any marsquakes observed so far.

- 732 3. The 2.4 Hz resonance. This resonance deserves its own category, because it has peculiar
733 characteristics. It was not observed when SEIS was recording while still on the lander (Pan-
734 ning et al., 2020), so it is not an obvious lander mode. While it has clear amplitude variations,
735 they are generally independent from variations in the broadband ambient noise that follow
736 general atmospheric patterns. For example, the 2.4 Hz resonance has a slightly higher excess
737 amplitude until Sol 200 and after Sol 450 (see Fig. 14). Further, it is sensitive to wind - but it
738 is not observed during high winds, and during a narrow range of moderate winds it appears
739 to increase in amplitude at a rate 300 times lower than the nearby 3.3 Hz lander mode, and
740 100 times lower than the background seismic noise (considering the components on which
741 each mode is strongest). It is not excited by the steady winds of the mornings between Sols
742 200 and 450 (in contrast to all lander modes previously described). Also in contrast to all
743 lander modes, it never disappears during quiet conditions (Figs. 1 and 8). This all suggests

744 an excitation mechanism, that (a) averages amplitudes over time scales and (b) is less ef-
745 fective than the lander modes. For an ergodic process, such as local, short duration wind
746 gusts (a) is equivalent to an averaging over regional scales. Since the topography of Elysium
747 Planitia around the landing site Homestead Hollow is extremely flat, there is no other object
748 as efficient as the lander in translating wind energy into ground motion nearby. A potential
749 explanation for the 2.4 Hz resonance is therefore, that it is part of the wind-driven ambient
750 noise in Elysium Planitia, caused mainly by wind friction on local topographic highs, such
751 as crater rims and exposed rocks. This mechanism averages contributions from many small
752 sources over time and space, but since it is less effective than the wind acting locally on
753 the lander and WTS, it is masked by this local wind noise during all but the quietest times.
754 Even more, the bulk of this ambient noise is below instrument noise at all times, and only
755 the 2.4 Hz peak is visible. This peak could be the result of a subsurface resonance, caused
756 by the layering of basaltic and sedimentary rocks with high impedance contrasts at the land-
757 ing site, as visible in outcrops in nearby impact craters (Golombek et al., 2020b; Pan et al.,
758 2020). An additional hint at a subsurface resonance is that the 2.4 Hz resonance is excited by
759 the majority of marsquakes, and specifically every marsquake with a source spectrum that
760 reaches above 2 Hz; this includes the so-called broadband events (Clinton et al., 2021) and
761 all events within the high-frequency family (van Driel et al., 2021). For these high-frequency
762 family events, we observe a hierarchy in amplitudes, with the strongest events showing a typ-
763 ical earthquake spectrum of a finite source plus attenuation of high frequencies modulated
764 by a Lorentz function centered at 2.4 Hz. For smaller events, the spectrum progressively
765 disappears below instrument noise, until for the weakest ones only the 2.4 Hz excitation is
766 observable. The observation that the polarization is continuous over time and identical for
767 high-frequency events and the ambient noise, is another hint that what controls the 2.4 Hz
768 resonance is mainly an effective anisotropy of the local subsurface and not an effect of the
769 seismic source. Our observations of the stable 2.4 Hz shape, both during ambient excitation
770 and events, are in agreement with the study by Compaire et al. (2021). In their autocor-
771 relation analysis based on the frequency band containing primarily the 2.4 Hz resonance,
772 the authors find reflected arrivals that are interpreted as vertically propagating P-waves and
773 weak, but consistent hints of S-wave arrivals.

774 In summary, it is therefore more akin to a basin resonance on Earth (Rial, 1989), which,
775 whether the seismic source is earthquakes (Flores et al., 1987) or environmental noise (Bodin
776 and Horton, 1999) shapes the local ambient seismic spectrum.

777 4. Temporary modes. There are a number of modes that were only present during specific time
778 frames of the mission (Fig. 4). For example, the 6.2 Hz mode is visible between Sols 258 and
779 298 (with a frequency shift on Sol 295, 6.2 to 5.9 Hz). This mode specifically appeared after
780 the IDA was placed into a parking position for the period around to the solar conjunction,
781 which coincided with a significant period of data loss. Another frequency that has been
782 observed only temporarily is at 3.7 Hz, which seems to appear when the IDA is above HP³.
783 The positions or specific actions of the IDA, e.g. the lifting of HP³ during Sol 203–209,
784 seem to be a driving force on the presence of temporary modes. During the lifting of HP³ in
785 particular, a large number of additional modes appear at 3 s, 1.2 Hz, 1.8 Hz, 1.9 Hz, 2.1 Hz,
786 2.4–2.6 Hz, 3.6 Hz, 3.9 Hz, 4.7 Hz, 5.1 Hz, 6.5–6.7 Hz, 7.6 Hz and 8.3 Hz. Further, modes
787 at 3.7 Hz and 2.7 Hz occur continuously following the HP³ deployment on Sol 76 and its
788 initial hammering session on Sol 92, respectively, and both stop once the housing is moved
789 on Sol 203. We suggest the 3.7 Hz mode is associated with the HP³ tether, and the 2.7 Hz
790 with vibrations of the HP³ frame that is temporally coupled to the ground via the partially
791 submerged and tilted mole.

792 Conclusion

793 In this manuscript we provide the first in-depth study of the spectral peaks observed in the contin-
794 uous InSight seismic dataset between 1 and 9 Hz. These peaks are a first-order feature of the data
795 and need to be considered in the analysis of the ambient noise or marsquake recordings to avoid
796 misinterpretation.

797 We track the major spectral peaks over large parts of the mission and quantify changes in their
798 peak frequency and spectral amplitude with temperature and wind, respectively. Spectral peaks
799 with completely stable peak frequencies and amplitudes occur at 1 Hz and harmonic overtones and
800 are produced by cross-talk, an artifact of the measurement system. A set of spectral peaks shows
801 strong variations with temperature and wind, or positions of the robotic arm, and consequently we

802 associate them with wind-excited reverberations of the lander system. The prominent broad 2.4 Hz
803 resonance shows amplitude variations over time, but is only comparatively weakly amplified by
804 local winds and has a stable peak frequency. Further, it is the only resonance that is excited by
805 marsquakes and could be produced by a local subsurface feature.

806 **Data and Resources**

807 The InSight seismic event catalog version 5 ([InSight Marsquake Service, 2021](#)), the waveform
808 data and station metadata are available from the IGP Datacenter and IRIS-DMC ([InSight Mars
809 SEIS Data Service, 2019b](#)), as are previous catalog versions. Seismic waveforms are also avail-
810 able from NASA PDS (National Aeronautics and Space Administration Planetary Data System,
811 <https://pds.nasa.gov/>, [InSight Mars SEIS Data Service \(2019a\)](#)). We use the 10 sps and 20 sps
812 channels from the VBB (channels 03.BH?, 02.BH?; "?" representing the three components UVW;
813 and the combined channel 58.BZC, where only the vertical component is transmitted at 10 sps) and
814 SP (68.SH?, 67.SH?) instruments, and for selected periods the 100 sps data (VBB: 00.HH?, SP:
815 65.EH?). The TWINS and scientific temperature (inside VBB and SP sensor assembly) are mainly
816 available sampled at 0.1–1 sps, atmospheric temperature (sensor 2: 20.LKO 1 sps, 20.VKO 0.5 sps,
817 23.VKO 0.1 sps), wind speed and direction (composite channels, speed/direction: 30.LWS/D 1 sps,
818 30.VWS/D 0.5 sps, 33.VWS/D 0.1 sps) and scientific temperature (02.VKI 0.2 sps, 03.VKI
819 0.1 sps). The channel location and codes follow an adapted version of the SEED (Standard for
820 the Exchange of Earthquake Data) naming convention. The seismic catalog ([InSight Marsquake
821 Service, 2021](#)) provides information on all detected events, including the event classification based
822 on frequency content, phase picks, back azimuth estimates, and event quality estimates (highest:
823 A, lowest: D). We use 32 *high frequency* events including S0319a and S0319b (all quality B,
824 implying multiple clear phases), and the *broadband* event S0235b (quality A: implying clear po-
825 larization and multiple clear phases, and hence location) from the InSight seismic event catalog
826 version 5 ([InSight Marsquake Service, 2021](#)). The data were processed with ObsPy ([Beyreuther
827 et al., 2010](#)), NumPy ([Harris et al., 2020](#)) and Scipy ([Virtanen et al., 2020](#)), and visualizations were
828 created with Matplotlib ([Hunter, 2007](#)), using scientific colormaps ([Crameri, 2020](#)) to prevent vi-
829 sual distortion of the data and exclusion of readers with color-vision deficiencies ([Crameri, 2018](#)).

830 The supplemental material includes data examples from the SP sensor, a mission-overview atmo-
831 spheric conditions (TWINS sensors), the polarization of the modes, and complementary analysis
832 of the 2.4 Hz amplitude variations.

833 **Glossary**

834 **Amazonian** Geological time period of Mars, approximately 3.0 Ga to present day.

835 **APSS** Auxiliary Payload Sensor Suite: a set of additional instruments to support the SEIS data
836 analysis. APSS consist of a Flux Gate magnetometer, an atmospheric pressure sensor, and
837 the subsystem TWINS.

838 **Donks** Transient, high frequency pulses in the seismic data. Predominantly, their energy is above
839 10 Hz and only occasionally these signals leak into the continuous 10 Hz data; can appear in
840 combination with glitches.

841 **dop** Degree of polarization.

842 **Glitches** Transient pulses in the seismic data which are thought to be caused by SEIS-internal
843 stress relaxations or tilts of the instrument. Glitches usually appear at frequencies below
844 1 Hz and with 25-30 s duration.

845 **Hesperian** Geological time period of Mars, approximately 3.8 Ga to 3.0 Ga.

846 **HF event** Type of seismic event with a broad excitation that includes the 2.4 Hz resonance as well
847 as higher frequencies; following the MQS event classification.

848 **HP³** Heat Flow and Physical Properties Package: set of instruments that were intended to measure
849 the heat flow in the near subsurface.

850 **IDA** Instrument Deployment Arm: InSight's robotic arm, designed to place the instruments on the
851 Martian Surface and used for other operational and scientific activities..

852 **InSight** Interior Exploration using Seismic Investigations, Geodesy and Heat Transport.

853 **Lander mode** Eigenmode of the lander, including any component of InSight, that produces a
854 spectral peak in the seismic data.

855 **LMST** Local Mean Solar Time at InSight landing site.

856 **LSA** Load Shunt Assembly: extra loop in the tether that connects SEIS with the lander. Designed
857 to mechanically decouple the SEIS-lander system.

858 **LVL** Leveling System: main, leveled structure on which the seismometers are located inside SEIS.

859 **Mole** Heat flow probe, part of the Heat Flow and Physical Properties Package.

860 **MQS** Marsquake Service: InSight mission group that is tasked with monitoring and cataloging
861 the Martian seismicity.

862 **NASA** National Aeronautics and Space Administration.

863 **Scientific temperature** Temperature measured within the VBB and SP sensor assembly.

864 **SEIS** Seismic Experiment for Interior Structure: SEIS consists of the co-located VBB and SP
865 seismometers within a thermal blanket located away from the lander, the electronic box
866 located on the lander, a tether linking these two components, and the WTS.

867 **Sol** Martian day counted from InSight's landing on November 26, 2018. A sol is equivalent to
868 ~24 h 40 min; the Martian year lasts about 668 sols.

869 **Solar conjunction** The period when the Sun is between the Earth and Mars. This leads to loss of
870 communication to the InSight lander, lasting for about 2 weeks.

871 **SP** Short Period seismometer: three-axis, micro-seismometer.

872 **Spectral peak** All peaks in the seismic spectrum which we associate with either mechanical lan-
873 der modes, ground resonances, or artifacts in the measurement system.

874 **sps** Samples per second.

875 **Tick noise** Artifact produced by crosstalk in the SEIS tether. The constant 1 Hz signal is visible
876 in spectra of the seismic data as a 1 Hz signal with harmonic overtones.

877 **TWINS** Temperature and Winds for InSight: Two sensor booms which measure the atmospheric
878 temperature and wind. They are mounted on the lander deck and face in opposite directions
879 outward over the solar panels.

880 **VBB** Very Broadband Seismometer: three-axis seismometer with oblique orientated components,
881 located within evacuated metal sphere.

882 **Whistling** A non-seismic signal artifact seen in spectra in the seismic data that is produced in the
883 electronics.

884 **WTS** Wind and Thermal Shield: the WTS provides thermal and wind protection for the SP and
885 VBB sensors.

886 **Acknowledgements**

887 We acknowledge NASA, CNES, their partner agencies and institutions (UKSA, SSO, DLR, JPL,
888 IPGP-CNRS, ETHZ, IC, MPS-MPG) and the flight operations team at JPL, SISMOC, MSDS,
889 IRIS-DMC and PDS for providing SEED SEIS data.

890 We acknowledge funding from (1) Swiss State Secretariat for Education, Research and Innovation
891 (SEFRI project “MarsQuake Service-Preparatory Phase”), (2) ETH Research grant ETH-06 17-
892 02, and (3) ETH+02 19-1: Planet MARS. The Swiss contribution in implementation of the SEIS
893 electronics was made possible through funding from the federal Swiss Space Office (SSO), the
894 contractual and technical support of the ESA-PRODEX office. The French authors acknowledge
895 the French Space Agency CNES and ANR (ANR-14-CE36-0012-02 and ANR-19-CE31-0008-08)
896 for support in the Science analysis.

897

898 This is InSight contribution 202.

899 **References**

- 900 Anderson, D. L., Miller, W., Latham, G., Nakamura, Y., Toksöz, M., Dainty, A., Duennebieer, F.,
901 Lazarewicz, A. R., Kovach, R., and Knight, T. (1977). Seismology on Mars, *J. Geophys. Res.*
902 82, no. 28, 4524–4546.
- 903 Banerdt, W. B., S. Smrekar, P. Lognonné, D. Giardini, M. Golombek, C. L. Johnson, P. Lognonné,
904 A. Spiga, T. Spohn, C. Perrin, et al. (2020). Initial results from the InSight mission: Surface
905 environment and global seismic activity, *Nature Geosci.* 13, 183–189, doi:10.1038/s41561-020-
906 0544-y.
- 907 Banfield, D., Rodriguez-Manfredi, J. A., Russell, C. T., Rowe, K. M., Leneman, D., Lai, H. R.,
908 Cruce, P. R., Means, J. D., Johnson, C. L., Mittelholz, A., et al. (2018). InSight Auxiliary
909 Payload Sensor Suite (APSS), *Space Sci. Rev.* 215, no. 1, 4., doi:10.1007/s11214-018-0570-x.
- 910 Banfield, D., Spiga, A., Newman, C., Forget, F., Lemmon, M., Lorenz, R., Murdoch, N., Viudez-
911 Moreiras, D., Pla-Garcia, J., Garcia, R. F., et al. (2020). The atmosphere of Mars as observed
912 by InSight, *Nat. Geosci.* 13, no. 3, 190–198, doi:10.1038/s41561-020-0534-0
- 913 Beyreuther, M., Barsch, R., Krischer, L., Megies, T., Behr, Y., and Wassermann, J. (2010).
914 ObsPy: A Python toolbox for seismology, *Seismol. Res. Lett.* 81, no. 3, 530–533, doi:
915 10.1785/gssrl.81.3.530.
- 916 Bodin, P. and Horton, S. (1999). Broadband microtremor observation of basin resonance
917 in the Mississippi Embayment, central US, *Geophys. Res. Lett.* 26, no. 7, 903–906,
918 doi:10.1029/1999GL900146.
- 919 Ceylan, S., J. Clinton, D. Giardini, M. Böse, C. Charalambous, M. van Driel, A. Horleston, T.
920 Kawamura, A. Khana, G. Orhand-Mainsant, et al. (2020). Companion guide to the Marsquake
921 catalog from InSight, sols 0–478: Data content and non-seismic events, *Phys. Earth Planet. In.*
922 310, doi:10.1016/j.pepi.2020.106597.
- 923 Charalambous, C., A. E. Stott, W. T. Pike, J. B. McClean, T. Warren, A. Spiga, D. Banfield, R.
924 F. Garcia, J. F. Clinton, S. C. Stähler, et al. (2021). A comodulation analysis of atmospheric

925 energy injection into the ground motion at InSight, Mars, *J. Geophys. Res.* 126, e2020JE006538,
926 doi:10.1029/2020JE006538.

927 Clinton, J. F., D. Giardini, M. Böse, S. Ceylan, M. van Driel, F. Euchner, R. F. Garcia, S. Kedar,
928 A. Khan, S. C. Stähler, et al. (2018). The Marsquake service: Securing daily analysis of SEIS-
929 data and building the Martian seismicity catalogue for InSight, *Space Sci. Rev.* 214, no. 8, 133,
930 doi:10.1007/s11214-018-0567-5.

931 Clinton, J. F., S. Ceylan, M. van Driel, D. Giardini, S. C. Stähler, M. Böse, C. Charalambous, N.
932 L. Dahmen, A. Horleston, T. Kawamura, et al. (2020). The Marsquake catalogue from InSight,
933 Sols 0-478, *Phys. Earth Planet In.* 310, doi:10.1016/j.pepi.2020.106595.

934 Compaire, N., Margerin, L., Garcia, R. F., Pinot, B., Calvet, M., Orhand-Mainsant, G., Kim,
935 D., Lekic, V., Tauzin, B., Schimmel, M., et al. (2021). Autocorrelation of the Ground Vi-
936 brations Recorded by the SEIS-InSight Seismometer on Mars, *J. Geophys. Res.* 126, no. 4,
937 e2020JE006498, doi:10.1029/2020JE006498.

938 Cramer, F. (2018). Geodynamic diagnostics, scientific visualisation and StagLab 3.0, *Geosci.*
939 *Model Dev.* 11, no. 6, 2541–2562, doi:10.5194/gmd-11-2541-2018.

940 Cramer, F. (2020). Scientific colour maps, doi:10.5281/zenodo.4153113

941 Fayon, L., Knapmeyer-Endrun, B., Lognonné P., Bierwirth, M., Kramer, A., Delage, P.,
942 Karakostas, F., Kedar, S., Murdoch, N., Garcia, R. F., et al. (2018). A numerical model of the
943 SEIS leveling system transfer matrix and resonances: Application to SEIS rotational seismology
944 and dynamic ground interaction, *Space Sci. Rev.* 214, no. 8, 11, doi:10.1007/s11214-018-0555-
945 9.

946 Flores, J., Novaro, O., and Seligman, T. H. (1987). Possible resonance effect in the distribution of
947 earthquake damage in Mexico City, *Nature*, 326, no. 6115, 783–785, doi:10.1038/326783a0.

948 Frankinet, B., Lecocq, T., and Camelbeeck, T. (2020). Wind-induced seismic noise at the Princess
949 Elisabeth Antarctica Station, *The Cryosphere Discuss.* 2020, 1–16, doi:/10.5194/tc-2020-267.

950 Giardini, D., P. Lognonné, W. Banerdt, W. Pike, U. Christensen, S. Ceylan, J. Clinton, M. van
951 Driel, S. Stähler, M. Böse, et al. (2020). The seismicity of Mars, *Nature Geosci.* 13, 1–8,
952 doi:10.1038/s41561-020-0539-8.

953 Golombek, M., Kass, D., Williams, N., Warner, N., Daubar, I., Piqueux, S., Charalambous, C., and
954 Pike, W. (2020a). Assessment of InSight Landing Site Predictions, *J. Geophys. Res.* 125, no. 8,
955 e2020JE006502, doi:10.1029/2020JE006502.

956 Golombek, M., Warner, N. H., Grant, J. A., Hauber, E., Ansan, V., Weitz, C. M., Williams, N.,
957 Charalambous, C., Wilson, S. A., DeMott, A., et al. (2020b). Geology of the InSight landing
958 site on Mars, *Nat Commun.* 11, no. 1, 1–11, doi:10.1038/s41467-020-14679-1.

959 Golombek, M., Williams, N., Warner, N. H., Parker, T., Williams, M. G., Daubar, I., Calef,
960 F., Grant, J., Bailey, P., Abarca, H., et al. (2020c). Location and Setting of the In-
961 Sight Lander, Instruments, and Landing Site, *Earth Space Sci.* 7, no. 10, e2020EA001248,
962 doi:10.1029/2020EA001248.

963 Harris, C. R., Millman, K. J., van der Walt, S. J., Gommers, R., Virtanen, P., Cournapeau, D.,
964 Wieser, E., Taylor, J., Berg, S., Smith, N. J., Kern, R., et al. (2020). Array programming with
965 NumPy, *Nature* 585, no. 7825, 357–362, doi:10.1038/s41586-020-2649-2.

966 Hunter, J. D. (2007). Matplotlib: A 2D graphics environment, *Comput. Sci. Eng.* 9, no. 3, 90–95,
967 doi:10.1109/MCSE.2007.55.

968 InSight Mars SEIS Data Service (2019a). InSight SEIS Data Bundle. PDS Geosciences (GEO)
969 Node, doi:10.17189/1517570.

970 InSight Mars SEIS Data Service (2019b). SEIS raw data, InSight Mission. IPGP, JPL, CNES,
971 ETHZ, ICL, MPS, ISAE-Supaero, LPG, MFSC, doi:10.18715/SEIS.INSIGHT.XB_2016.

972 InSight Marsquake Service (2021). Mars Seismic Catalogue, InSight Mission; V5 2021-01-04.
973 ETHZ, IPGP, JPL, ICL, ISAE-Supaero, MPS, Univ Bristol. Dataset, doi:10.12686/a10.

974 Johnson, C. L., Mittelholz, A., Langlais, B., Russell, C. T., Ansan, V., Banfield, D., Chi, P. J.,
975 Fillingim, M. O., Forget, F., Haviland, H. F., et al. (2020). Crustal and time-varying magnetic

976 fields at the InSight landing site on Mars, *Nat Geosci.* 13, no. 3, 199–204, doi:10.1038/s41561-
977 020-0537-x.

978 Johnson, C. W., Meng, H., Vernon, F., and Ben-Zion, Y. (2019). Characteristics of ground motion
979 generated by wind interaction with trees, structures, and other surface obstacles, *J. Geophys.*
980 *Res.* 124, no. 8, 8519–8539, doi:10.1029/2018JB017151.

981 Virtanen, P., Gommers, R., Oliphant, T.E. et al. (2020) SciPy 1.0: fundamental algorithms for
982 scientific computing in Python, *Nat. Methods* 17, 261–272, doi:10.1038/s41592-019-0686-2

983 Latham, G. V., Ewing, M., Press, F., Sutton, G., Dorman, J., Nakamura, Y., Toksoz, N., Wiggins,
984 R., Derr, J., and Duennebier, F. (1970a). Apollo 11 passive seismic experiment, *Proc. Apollo 11*
985 *Lunar Sci. Conf.* 2309-2320.

986 Latham, G. V., Ewing, M., Press, F., Sutton, G., Dorman, J., Nakamura, Y., Toksöz, N., Wiggins,
987 R., Derr, J., and Duennebier, F. (1970b). Passive seismic experiment, *Science* 167, no. 3918,
988 455–457.

989 Lognonné, P., W. B. Banerdt, D. Giardini, W. T. Pike, U. Christensen, P. Laudet, S. de Raucourt, P.
990 Zweifel, S. Calcutt, M. Bierwirth, et al. (2019). SEIS: InSight’s seismic experiment for internal
991 structure of Mars, *Space Sci. Rev.* 215, no. 1, 12, doi:10.1007/s11214-018-0574-6.

992 Lognonné, P., W. B. Banerdt, D. Giardini, W. T. Pike, U. Christensen, R. F. Garcia, T. Kawamura, S.
993 Kedar, B. Knapmeyer-Endrun, L. Margerin, et al. (2020). Constraints on the shallow elastic and
994 anelastic structure of Mars from InSight data, *Nature Geosci.* 13, 213–220, doi:10.1038/s41561-
995 020-0536-y.

996 Lognonné, P. and Mosser, B. (1993). Planetary seismology, *Surv. Geophys.* 14, no. 3, 239–302.

997 Mimoun, D., N. Murdoch, P. Lognonné, K. Hurst, W. T. Pike, J. Hurley, T. Nebut, and W. B.
998 Banerdt (2017). The noise model of the SEIS seismometer of the InSight mission to Mars,
999 *Space Sci. Rev.* 211, 383–428, doi:10.1007/s11214-017-0409-x.

1000 Mueller, N. T., Knollenberg, J., Grott, M., Kopp, E., Walter, I., Krause, C., Hudson, T., Spohn, T.,
1001 and Smrekar, S. (2020). Calibration of the HP3 Radiometer on InSight, *Earth Space Sci.* 7, no.
1002 5, e2020EA001086, doi:10.1029/2020EA001086.

- 1003 Murdoch, N., Alazard, D., Knapmeyer-Endrun, B., Teanby, N., and Myhill, R. (2018). Flexible
1004 mode modelling of the InSight lander and consequences for the SEIS instrument, *Space Sci.*
1005 *Rev.* 214, no. 8, 117, doi:10.1007/s11214-018-0553-y.
- 1006 Murdoch, N., Mimoun, D., Garcia, R. F., Rapin, W., Kawamura, T., Lognonné, P., Banfield, D.,
1007 and Banerdt, W. B. (2017). Evaluating the Wind-Induced Mechanical Noise on the InSight
1008 Seismometers, *Space Sci. Rev.* 211, no. 1-4, 429–455, doi:10.1007/s11214-016-0311-y.
- 1009 Myhill, R., Teanby, N., Wookey, J., and Murdoch, N. (2018). Near-field seismic propagation and
1010 coupling through Mars' regolith: implications for the InSight Mission, *Space Sci. Rev.* 214, no.
1011 5, 85, doi:10.1007/s11214-018-0514-5.
- 1012 Pan, L., Quantin-Nataf, C., Tauzin, B., Michaut, C., Golombek, M., Lognonné, P., Grindrod, P.,
1013 Langlais, B., Gudkova, T., Stepanova, I., et al. (2020). Crust stratigraphy and heterogeneities of
1014 the first kilometers at the dichotomy boundary in western Elysium Planitia and implications for
1015 InSight lander, *Icarus* 338, 113511, doi:10.1016/j.icarus.2019.113511.
- 1016 Panning, M. P., Pike, W. T., Lognonné, P., Banerdt, W. B., Murdoch, N., Banfield, D., Char-
1017 alambous, C., Kedar, S., Lorenz, R. D., Marusiak, A. G., et al. (2020). On-Deck Seismology:
1018 Lessons from InSight for Future Planetary Seismology, *J. Geophys. Res.* 125, no. 4, 1–13,
1019 doi:10.1029/2019JE006353.
- 1020 Paz, M., Kim, Y. H. (2019). *Structural dynamics: Theory and Computation (6th edition)*, Springer
1021 Nature Switzerland AG, Cham, P. 55-57.
- 1022 Rial, J. A. (1989). Seismic wave resonances in 3D sedimentary basins, *Geophys. J. Int.* 99, no. 1,
1023 81–90, doi:10.1111/j.1365-246X.1989.tb02016.x.
- 1024 Samson, J. (1980). Comments on polarization and coherence, *Journal of Geophysics - Zeitschrift*
1025 *für Geophysik* 48, no. 3, 195–198.
- 1026 Samson, J. (1983). Pure states, polarized waves, and principal components in the spectra of multi-
1027 ple, geophysical time-series, *Geophys. J. Int.* 72, no. 3, 647–664.

- 1028 Savoie, D., Richard, A., Goutaudier, M., Lognonné, P., Hurst, K., Maki, J. N., Golombek, M. P.,
1029 van Driel, M., Clinton, J., Stutzmann, E., et al. (2021). Finding SEIS North on Mars: Compar-
1030 isons between SEIS sundial, Inertial and Imaging measurements and consequences for seismic
1031 analysis, *Earth Space Sci.* 8, no. 3, e2020EA001286, doi:10.1029/2020EA001286.
- 1032 Schimmel, M. and Gallart, J. (2003). The use of instantaneous polarization attributes for
1033 seismic signal detection and image enhancement, *Geophys. J. Int.* 155, no. 2, 653–668,
1034 doi:10.1046/j.1365-246X.2003.02077.x.
- 1035 Schimmel, M. and Gallart, J. (2004). Degree of polarization filter for frequency-dependent sig-
1036 nal enhancement through noise suppression, *Bull. Seismol. Soc. Am.* 94, no. 3, 1016–1035,
1037 doi:10.1785/0120030178.
- 1038 Schimmel, M., Stutzmann, E., Lognonné, P., Compaire, N., Davis, P., Drilleau, M., Garcia, R. ,
1039 Kim, D., Knapmeyer-Endrun, B., Lekic, V., et al. (2021). Seismic noise autocorrelations on
1040 Mars, *Earth Space Sci.* 8, no. 6, e2021EA001755, doi:10.1029/2021EA001755.
- 1041 Scholz, J.-R., Widmer-Schmidrig, R., Davis, P., Lognonné, P., Pinot, B., Garcia, R. F., Hurst,
1042 K., Pou, L., Nimmo, F., Barkaoui, S., et al. (2020). Detection, analysis, and removal of
1043 glitches from InSight’s seismic data from Mars, *Earth Space Sci.* 7, no. 11, e2020EA001317,
1044 doi:10.1029/2020EA001317.
- 1045 Spiga, A., Banfield, D., Teanby, N. A., Forget, F., Lucas, A., Kenda, B., Manfredi, J. A. R.,
1046 Widmer-Schmidrig, R., Murdoch, N., Lemmon, M. T., et al. (2018). Atmospheric science with
1047 InSight, *Space Sci. Rev.* 214, no. 7, 109, doi:10.1007/s11214-018-0543-0.
- 1048 Spohn, T., Grott, M., Smrekar, S., Knollenberg, J., Hudson, T., Krause, C., Müller, N., Jänchen, J.,
1049 Börner, A., Wippermann, T., et al. (2018). The heat flow and physical properties package (HP
1050 3) for the InSight mission, *Space Sci. Rev.* 214, no. 5, 96, doi:10.1007/s11214-018-0531-4.
- 1051 Stähler, S. C., Widmer-Schmidrig, R., Scholz, J.-R., van Driel, M., Mittelholz, A., Hurst, K.,
1052 Johnson, C. L., Lemmon, M. T., Lognonné, P., Lorenz, R., et al. (2020). Geophysical ob-
1053 servations of Phobos transits by InSight, *Geophys. Res. Lett.* 47, no. 19, e2020GL089099,
1054 doi:10.1029/2020GL089099.

- 1055 Stott, A., Charalambous, C., McClean, J., Warren, T., Trebi-Ollennu, A., Lim, G., Teanby, N.,
1056 Myhill, R., Horleston, A., Kedar, S., et al. (2020). Using InSight's Robotic Arm Motion to
1057 Examine the Martian Regolith's Response to Short Period Vibrations, In *Lunar and Planetary*
1058 *Science Conference* No. 2326, id. 2082.
- 1059 Stutzmann, E., Schimmel, M., Lognonné, P., Horleston, A., Ceylan, S., van Driel, M., Stahler, S.,
1060 Banerdt, B., Calvet, M., Charalambous, C., et al. (2021). The polarization of ambient noise on
1061 Mars, *J. Geophys. Res.* 126, no. 1, e2020JE006545, doi:10.1029/2020JE006545.
- 1062 Trebi-Ollennu, A., Kim, W., Ali, K., Khan, O., Sorice, C., Bailey, P., Umland, J., Bonitz, R.,
1063 Ciarleglio, C., Knight, J., et al. (2018). InSight Mars Lander Robotics Instrument Deployment
1064 System, *Space Sci. Rev.* 214, no. 5, 93, doi:10.1007/s11214-018-0520-7.
- 1065 van Driel, M., S. Ceylan, J. F. Clinton, D. Giardini, A. Horleston, L. Margerin, S. C. Stähler, M.
1066 Böse, C. Charalambous, T. Kawamura, et al. (2021). High-frequency seismic events on Mars
1067 observed by InSight, *J. Geophys. Res.* 126, e2020JE006670, doi:10.1029/2020JE006670.
- 1068 Warner, N., Grant, J., Wilson, S., Golombek, M., DeMott, A., Charalambous, C., Hauber, E.,
1069 Ansan, V., Weitz, C., Pike, T., et al. (2020). An Impact Crater Origin for the InSight Landing
1070 Site at Homestead Hollow, Mars: Implications for Near Surface Stratigraphy, Surface Processes,
1071 and Erosion Rates, *J. Geophys. Res.* 125, no. 4, e2019JE006333, doi:10.1029/2019JE006333.
- 1072 Zweifel, P., Mance, D., ten Pierick, J., Giardini, D., Schmelzbach, C., Haag, T., Nicollier, T., and
1073 S., C. (2021). Seismic High-Resolution Acquisition Electronics for NASA InSight mission on
1074 Mars, Submitted to Bull. Seismol. Soc. Am..

1075 **Author affiliations**

1076 ¹ Nikolaj L. Dahmen, Institute of Geophysics, ETH Zurich, NO E 17, Sonneggstrasse 5, 8092
1077 Zurich, Switzerland

1078 ² Géraldine Zenhäusern, Institute of Geophysics, ETH Zurich, NO E 17, Sonneggstrasse 5, 8092
1079 Zurich, Switzerland

1080 ³ John F. Clinton, Swiss Seismological Service (SED), ETH Zurich, NO FO 69.3, Sonneggstrasse
1081 5, 8092 Zurich, Switzerland

1082 ⁴ Domenico Giardini, Institute of Geophysics, ETH Zurich, NO H 69.1, Sonneggstrasse 5, 8092
1083 Zurich, Switzerland

1084 ⁵ Simon C. Stähler, Institute of Geophysics, ETH Zurich, NO H 53.2, Sonneggstrasse 5, 8092
1085 Zurich, Switzerland

1086 ⁶ Savas Ceylan, Institute of Geophysics, ETH Zurich, NO F 5, Sonneggstrasse 5, 8092 Zurich,
1087 Switzerland

1088 ⁷ Constantinos Charalambous, 706, Electrical and Electronic Engineering, South Kensington Cam-
1089 pus, Imperial College London, London SW7 2AZ, Greater London, United Kingdom

1090 ⁸ Martin van Driel, Institute of Geophysics, ETH Zurich, NO J 44, Sonneggstrasse 5, 8092 Zurich,
1091 Switzerland

1092 ⁹ Kenneth J. Hurst, Jet Propulsion Laboratory, 4800 Oak Grove Drive, M/S 264-528, Pasadena,
1093 CA 91109, United States

1094 ¹⁰ Sharon Kedar, Jet Propulsion Laboratory, 4800 Oak Grove Drive, M/S 238-600, Pasadena, CA
1095 91109, United States

1096 ¹¹ Philippe Lognonné, Université Paris Diderot, Institut de Physique du Globe de Paris, 35 rue
1097 Hélène Brion, Case 7071, Lamarck A, 75205 Paris Cedex 13, France

1098 ¹² Naomi Murdoch, ISAE-SUPAERO, Université de Toulouse, DEOS/Space Systems for Plane-
1099 tary Applications, 10 avenue Edouard Belin, BP 54032, 31055 Toulouse Cedex 4, France, Office
1100 ISAE: 07-1129

1101 ¹³ Robert Myhill, University of Bristol, School of Earth Sciences, BS8 1RJ, United Kingdom

1102 ¹⁴ Mark P. Panning, Jet Propulsion Laboratory, 4800 Oak Grove Drive, M/S 183-301, Pasadena,
1103 CA 91109, United States

1104 ¹⁵ William T. Pike, 604, Electrical Engineering, South Kensington Campus, Imperial College Lon-

1105 don, London SW7 2AZ, Greater London, United Kingdom

1106 ¹⁶ Martin Schimmel, Geosciences Barcelona, GEO3BCN - CSIC, Lluís Sole i Sabaris s/n, 08028
1107 Barcelona, Spain.

1108 ¹⁷ Cédric Schmelzbach, Institute of Geophysics, ETH Zurich, NO H 44, Sonneggstrasse 5, 8092
1109 Zurich, Switzerland

1110 ¹⁸ John-Robert Scholz, Max-Planck-Institut für Sonnensystemforschung, Justus-von-Liebig-Weg
1111 3, 37077 Göttingen, Germany

1112 ¹⁹ Alexander E. Stott, ISAE-SUPAERO, Université de Toulouse, DEOS/Space Systems for Plane-
1113 tary Applications, 10 avenue Edouard Belin, BP 54032, 31055 Toulouse Cedex 4, France

1114 ²⁰ Eleonore Stutzmann, Université de Paris, Institut de Physique du Globe de Paris, CNRS, 1 rue
1115 Jussieu, 75005 Paris, France

1116 ²¹ William B. Banerdt, Jet Propulsion Laboratory, 4800 Oak Grove Drive, M/S 264-528, Pasadena,
1117 CA 91109, United States

Table 1: Occupations of Instrument Deployment Arm (IDA) between Sol 74-650 as shown in Figure 4.

IDA occupation	Occurrence [Sol]
1) Grapple holding HP ³ housing	74-75, 77-83, 190-203, 210-223
2) Above HP ³ - grapple out	84-95, 182-189, 224-227
3) Over lander deck or miscellaneous positions	96-102, 106-109, 112-126, 133-146, 149-154, 160-181, 296-297, 578-597
4) Above HP ³ - grapple secured	103-105, 110-111, 127-132, 147-148, 155-159, 228-239, 298-302, 332-335, 418-434, 598-611
5) Lifting HP ³ housing	76, 204-209
6) Digging (pressing scoop into ground and lifting up again)	240-257
7) Next to western lander leg (parking position for solar conjunction)	258-295
8) Solar conjunction (no data available)	268-288
9) Pinning heat flow probe (mole)	303-331, 336-417, 435-577, 612-650

1118 **Tables**

Table 2: Characteristics of main lander modes, 2.4 Hz resonance, and tick noise.

Name	Frequency range [Hz]	Spectral width [Hz]	Damping ratios [%] - Sol 319	Frequency variation with atmospheric temperature	Amplitude variation with local wind - combined components / velocity [dB]	Variation of azimuth [degree]	Distribution on components (Z=vertical, N=north, E=east)	When visible?	Other characteristics	Likely origin
1.6 Hz	1.4-1.7	n/a	1.27-1.32	minor (5-10%)	-205 to -175	night: 325 day: not tracked	strongest on E,N	winds <7 m/s	possibly retrograde hysteresis	lander
3.3 Hz	3.0-3.3	0.02-0.10	0.64-0.69	minor (5-10%)	-205 to -160	night: 320 day: 350; during very windy periods: ~220	strongest on E,N	all windy periods		lander
4.1 Hz	3.8-4.1	0.05-0.10	0.86-0.98	minor (5-10%)	-200 to -140	night: 260-290 day: 210-250	strongest on E, then Z, then N	all windy periods	stronger vertical polarization component (inclination up to 30°)	lander
6.8 Hz	5.8-6.9	0.05-0.10	0.49-0.53	moderate (10-15%)	-200 to -150	night: 270-300 day: 220-260	strongest on E,N	all windy periods		lander
8.6 Hz	6.5-8.6	n/a	0.64	strong (20%)	-195 to -160	night: 300 day: 260	strongest on E,N	winds <10 m/s		lander
2.4 Hz	2.4-2.6	0.3-0.4	4.22	none	amplitude modulated by background noise level	centered around 180 (150-210) (value depends on processing and might not be stable)	strongest on Z	winds <5 m/s	- complex peak structure: Z: 2.4 Hz and smaller peak at 2.35 Hz, N: 2.35 and 2.5Hz; E: 2.6 Hz; - excited by seismic events	subsurface
Tick noise	1.0	1 mHz	none	none	amplitude modulated by background noise level	none	Related to original components: highest amplitude on VBB V	quiet periods	harmonic overtones at multiples of 1 Hz	measurement system

1119 **List of figure captions**

1120 Figure 1: InSight data collected on Sol 319. (a) Wind speed from composite channel (black),
1121 with reliability threshold 1.8–2.8 m/s (red-dashed); (b) atmospheric temperature from composite
1122 channel (black) and SP sensor temperature inside the VBB and SP sensor assembly (but outside
1123 of the sphere containing the VBB, blue-dashed); the spectrograms from the (c) 100 sps SP vertical
1124 component, and 20 sps VBB (d) vertical, (e) north and (f) east components. Spectrograms are
1125 computed with a window length of 120 s windows and 50% overlap. Sunrise and sunset times are
1126 indicated by the vertical orange-dotted lines (a)-(b) or orange triangles (c)-(f).

1127

1128 Figure 2: Spectra from 20 sps VBB data. (a) Vertical, (b) north and (c) east component, com-
1129 puted with 120 s windows and 50% overlap. Shown are the daily mean spectra from 0–5 LMST
1130 during the period Sol 183–192 (colored lines), and their total mean (black line). Shaded vertical
1131 bars mark the individual modes.

1132

1133 Figure 3: SP sensor on deck. Spectra computed from the 100 sps SP data on Sol 20 around
1134 21:00 LMST, computed with 120 s windows and 50% overlap; color bars indicate the expected
1135 frequency range of the 1.6 Hz, 3.3 Hz, 4.1 Hz, 6.8 Hz and 8.6 Hz modes at atmospheric tempera-
1136 ture of ~ 200 K, estimated from the values observed by the seismometer on ground.

1137

1138 Figure 4: Summary of IDA position and temporary modes observed between Sols 75–650. Black
1139 lines denote the robotic arm position in the IDA reference frame (a) x , (b) y , (c) z , (d) th . ‘enc’
1140 refers to encoder measurements. Slanted lines reflect long gaps without the arm position infor-
1141 mation. The red lines indicate the identified temporary modes. The background color gives the
1142 general IDA occupation: 1) Grapple holding HP³ housing, 2) Above HP³ - grapple out, 3) Over
1143 lander deck or miscellaneous positions, 4) Above HP³ - grapple secured, 5) Lifting HP³ housing,
1144 6) Digging, 7) Next to western lander leg (parking position), 8) Solar conjunction, 9) Pinning the
1145 the heat flow probe. The exact time intervals are given in Table 1.

1146

1147 Figure 5: Comparison of VBB and SP seismometers. Spectra from Sol 422 for the (a) vertical
1148 (with inset (b) focusing on the frequency range from 0–15 Hz at lowest amplitudes), (c) north

1149 and (d) east components, computed with 120 s windows and 50% overlap. Data are taken from
1150 the night period 3:30–5:30 LMST (a period with steady but light winds) and the evening period
1151 20:30–22:30 LMST (quietest period of the day).

1152

1153 Figure 6: Frequency variation of modes with temperature. Averaged spectra by atmospheric
1154 temperature (sensor 2) on VBB (a) vertical, (b) north and (c) east component, computed with 120 s
1155 windows and 50% overlap. Each line corresponds to an average over 130 h, randomly selected
1156 from Sol 182–500. Highlighted are the frequency ranges of the 2.4 Hz (blue) and 1.6 Hz, 3.3 Hz,
1157 4.1 Hz and 6.8 Hz modes (red).

1158

1159 Figure 7: Polarization analysis Sol 319, VBB. (a) Three-component scalogram, (b) ellipticity,
1160 (c) major azimuth, and (d) major inclination, shown up to 9 Hz, computed with 120 s window
1161 length. The degree of polarization filter applied in (b)-(d) (with 120s window length, 0.05 Hz
1162 spectral width) removes all signals with degree of polarization values below 0.4.

1163

1164 Figure 8: Tracking spectral peaks on Sol 319. The background shows the three-component
1165 scalogram from the 20sps VBB sensor, with 300s window length and 50% overlap. Solid green
1166 lines: automatically picked modes and tick noise, dotted green lines: manually picked modes.

1167

1168 Figure 9: (a) Diurnal changes of atmospheric temperature measured by sensor 1 for different
1169 sols spread across the mission, from Sol 185 to Sol 625. (b)-(h) Diurnal changes in the natural
1170 frequency of modes for the same sols. (b) presents all modes plus the 1 Hz tick noise in a single
1171 figure, from 0–10 Hz. (c)-(h) show each mode in more detail. Depicted are both the automatically
1172 tracked signals (2.4 Hz (g), 3.3 Hz (f), 4.1 Hz (e), 6.8 Hz (d)) and the manually tracked modes
1173 (1.6 Hz (h), 8.6 Hz (c)). Note the inverse y-axis for (a).

1174

1175 Figure 10: Variations of tracked spectral peaks across the entire mission. (a) Spectral peaks from
1176 the three-component scalogram at representative times individually selected where the peaks are
1177 clearly observed. Histograms of (b) the peak frequency against atmospheric temperature and (c)
1178 spectral amplitude against wind over the mission (Sol 182–649, where available). Depicted are the

1179 1 Hz tick noise, and 1.6 Hz, 2.4 Hz, 3.3 Hz, 4.1 Hz, 6.8 Hz, and 8.6 Hz modes. Temperature sensor
1180 1, and wind composite data are used. Note the different y-axes and log color scales between modes.

1181

1182 Figure 11: Variations of tracked spectral peaks across Sol 319. (left) Relative frequency (nor-
1183 malized with respect to frequency at 170 K) against atmospheric temperature and (right) amplitude
1184 against wind for all tracked peaks. (a,b) 1 Hz tick noise, (c,d) 1.6 Hz, (e,f) 2.4 Hz, (g,h) 3.3 Hz,
1185 (i,j) 4.1 Hz, (k,l) 6.8 Hz, and (m,n) 8.6 Hz modes. Colors on the left indicate time of day, colors
1186 on the right give the wind direction. Note the logarithmic x-axis on the right.

1187

1188 Figure 12: Overview of the VBB sensitivity to temperature (a)-(c) and wind (d)-(f), with focus
1189 on the 2.4 Hz resonance and 3.3 Hz lander mode. (a)-(c) show lines of average velocity spectra
1190 for each component of VBB binned by similar atmospheric temperatures (using sensor 1) on (a)
1191 logarithmic, (b) linear, and (c) linear scale with broadband noise baseline removed. The inset in
1192 (c) focuses on the 2.4 Hz resonance. Each binned line represents approx. 38 h of data with similar
1193 temperatures collected between Sols 182-650. (d)-(f) presents a similar analysis for wind speed.
1194 (d) is on a logarithmic scale, (e) linear scale, and (f) linear scale with baseline of broadband noise
1195 removed. The inset in (f) focuses on the 2.4 Hz resonance though only includes wind speeds up
1196 to 6 m/s. Each line represents between 118 h (low wind speeds) and 350 h (high wind speeds) of
1197 data, collected between Sol 182-500. Spectra are computed with 120 s window length. For the
1198 baseline, a linear fit of the average power values between 1.75-1.85 Hz to 2.75-2.85 Hz is removed
1199 for each binned spectrum. This line is indicated in (e), for the highest wind speed only.

1200

1201 Figure 13: Correlation of the VBB amplitudes from the 2.4 Hz resonance (a) and 3.3 Hz lander
1202 mode (b) with wind speed. At each frequency and VBB component, we plot the excess power
1203 in velocity for each wind speed, extracted from Figure 12 (f) (these values include the baseline
1204 removal of the noise by subtracting a linear fit between averages of 1.75-1.85 and 2.75-2.85 Hz).
1205 (a) shows the excess power of the 2.4 Hz resonance and 2 Hz tick noise overtone in different wind
1206 conditions. (b) shows the excess power of the 3.3 Hz lander mode and increase of broadband noise
1207 level, using 1.8 Hz and 2.8 Hz as a proxy. A linear reference line between 3.75-7.5 m/s (black-
1208 dotted line) is given for the vertical component in (a), and the 3.3 Hz lander mode for the north

1209 component in (b), and additionally, for the broadband noise at 1.8 Hz and 2.8 Hz. The markers
1210 are slightly offset on the x-axis to avoid overlaps; the vertical gray lines mark wind measurements
1211 of 1.8 and 2.8 m/s, speeds below these levels are considered unreliable. The values represent the
1212 average excess power in a 0.1 Hz frequency bin around 2.4 Hz (Z), 2.5 Hz (N) and 2.6 Hz (E);
1213 and a 0.1 Hz bin around the varying peak of the 3.3 Hz mode. Additionally, we use a 0.05 Hz bin
1214 around 2 Hz, and 0.1 Hz bin around both 1.8 Hz and 2.8 Hz. The uncertainties are indicated by the
1215 min./max. values in these frequency ranges.

1216

1217 Figure 14: Seasonal variations in amplitude of VBB 2.4 Hz resonance. Shown is the vertical
1218 component (channels 58.BZC, 02/03.BHZ, see Data and Resources), extracted from a frequency
1219 band around 2.3–2.5 Hz, for the period Sol 70–650. Only periods when the amplitude in the
1220 2.2–2.6 Hz band exceeds the broadband amplitude (1.2–3.0 Hz) by 6 dB are indicated. The energy
1221 onset times of 32 high quality, *high frequency* (HF) events with strong 2.4 Hz excitation are marked
1222 (see Data and Resources). The start of the seasons on the northern (N.) hemisphere, where InSight
1223 is located, are also indicated. Note no data are available during the solar conjunction.

1224

1225 Figure 15: Overview of the excitation of the 2.4 Hz resonance during 32 *high frequency* events.
1226 The velocity spectra (30 s window length) are computed over the main S-wave energy for the (a)
1227 vertical, (c) north and (e) east components. The mean from all events (red) as well as from all pre-
1228 event time windows (red-dotted) are indicated. The spectral difference between each event and
1229 the pre-event signal is shown for the (b) vertical, (d) north and (f) east components. The vertical
1230 black-dotted line marks the 2.4 Hz frequency.

1231

1232 Figure 16: Polarization analysis for high quality, teleseismic event S0235b. (a) Three-component
1233 scalogram, and histograms of (b) a pre-event noise and (c) a signal time window. (d) Azimuth and
1234 (e), (f) respective histograms. We use the continuous wavelet transform and apply a degree of
1235 polarization filter that removes signals with degree of polarization values below 0.4. The signal
1236 window is taken as -20 to +110 s around the P arrival. Black horizontal lines in (b), (c), (e), and (f)
1237 mark the boundaries of the 2.4 Hz resonance. A dashed vertical line in (f) marks the MQS catalog
1238 back azimuth for the event.

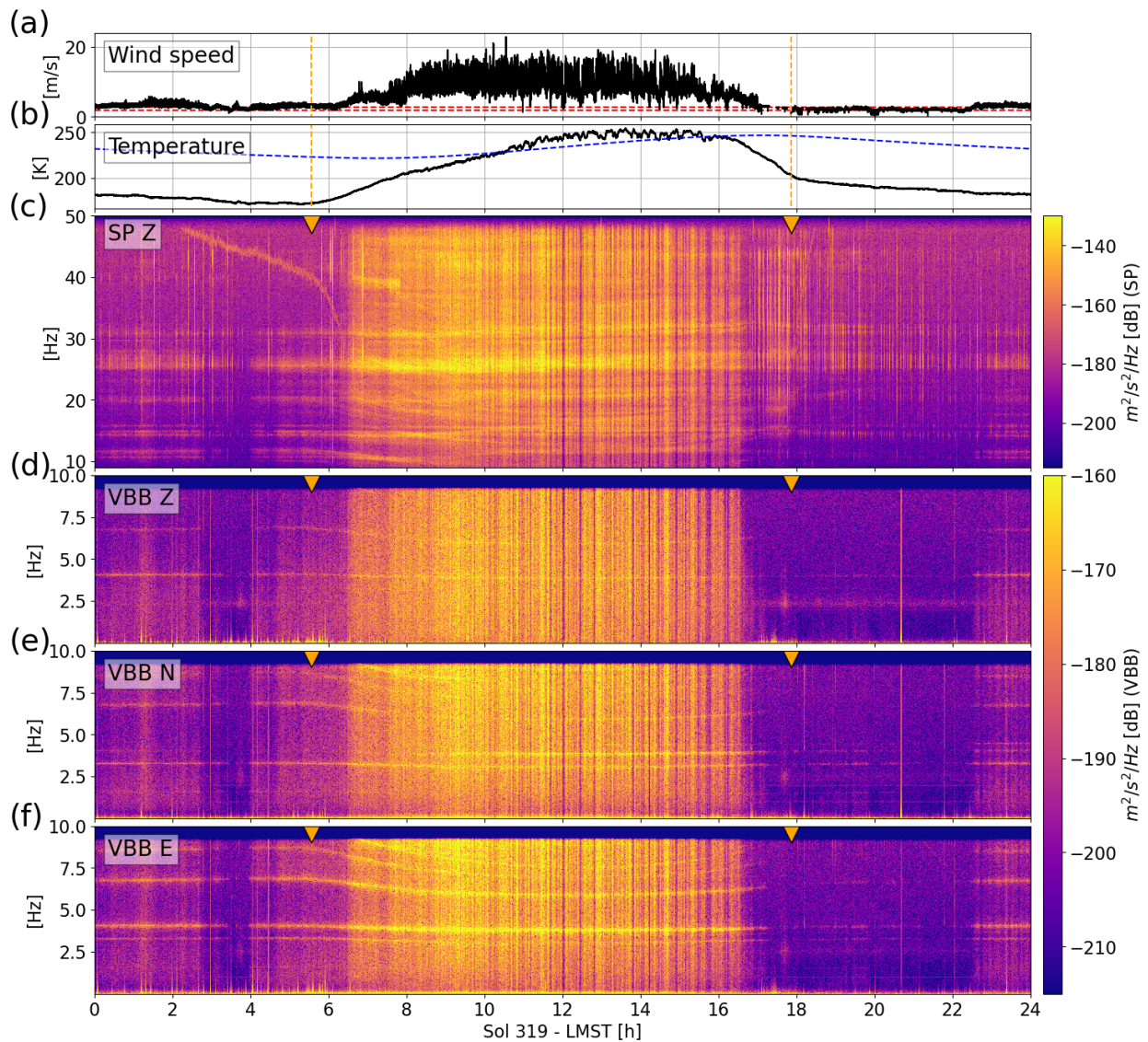


Figure 1. InSight data collected on Sol 319. (a) Wind speed from composite channel (black), with reliability threshold 1.8–2.8 m/s (red-dashed); (b) atmospheric temperature from composite channel (black) and SP sensor temperature inside the VBB and SP sensor assembly (but outside of the sphere containing the VBB, blue-dashed); the spectrograms from the (c) 100 sps SP vertical component, and 20 sps VBB (d) vertical, (e) north and (f) east components. Spectrograms are computed with a window length of 120 s windows and 50% overlap. Sunrise and sunset times are indicated by the vertical orange-dotted lines (a)-(b) or orange triangles (c)-(f).

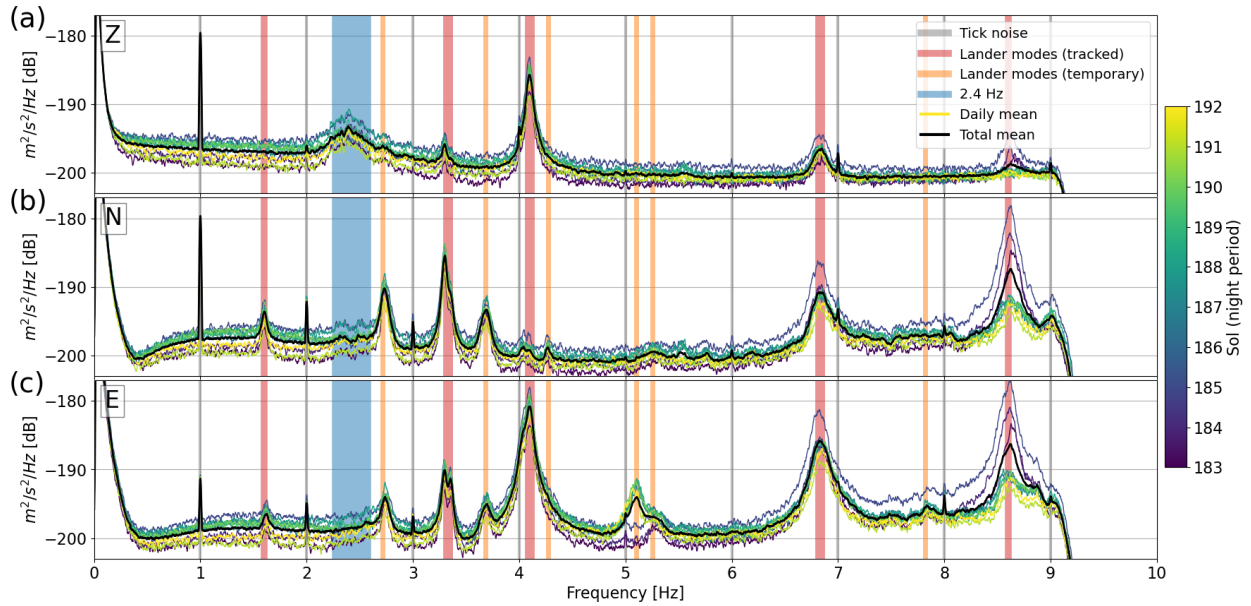


Figure 2. Spectra from 20 sps VBB data. (a) Vertical, (b) north and (c) east component, computed with 120 s windows and 50% overlap. Shown are the daily mean spectra from 0–5 LMST during the period Sol 183–192 (colored lines), and their total mean (black line). Shaded vertical bars mark the individual modes.

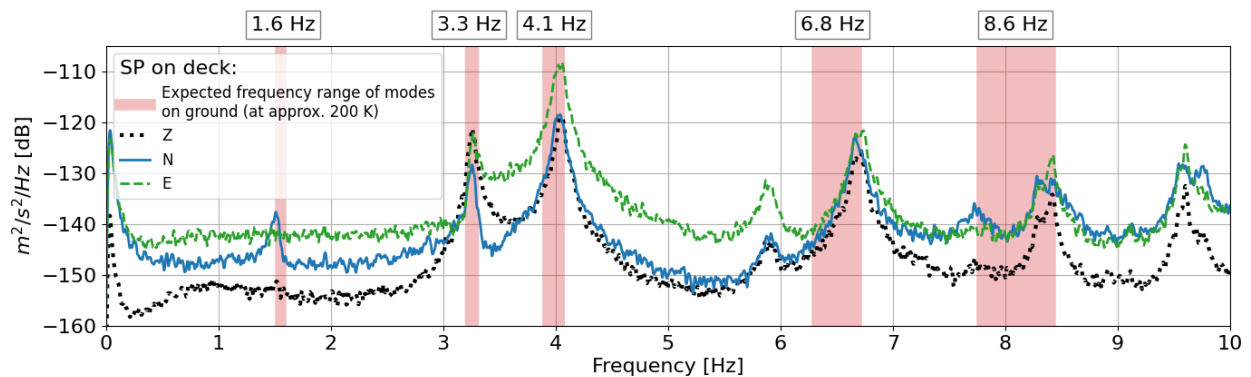


Figure 3. SP sensor on deck. Spectra computed from the 100 sps SP data on Sol 20 around 21:00 LMST, computed with 120 s windows and 50% overlap; color bars indicate the expected frequency range of the 1.6 Hz, 3.3 Hz, 4.1 Hz, 6.8 Hz and 8.6 Hz modes at atmospheric temperature of ~ 200 K, estimated from the values observed by the seismometer on ground.

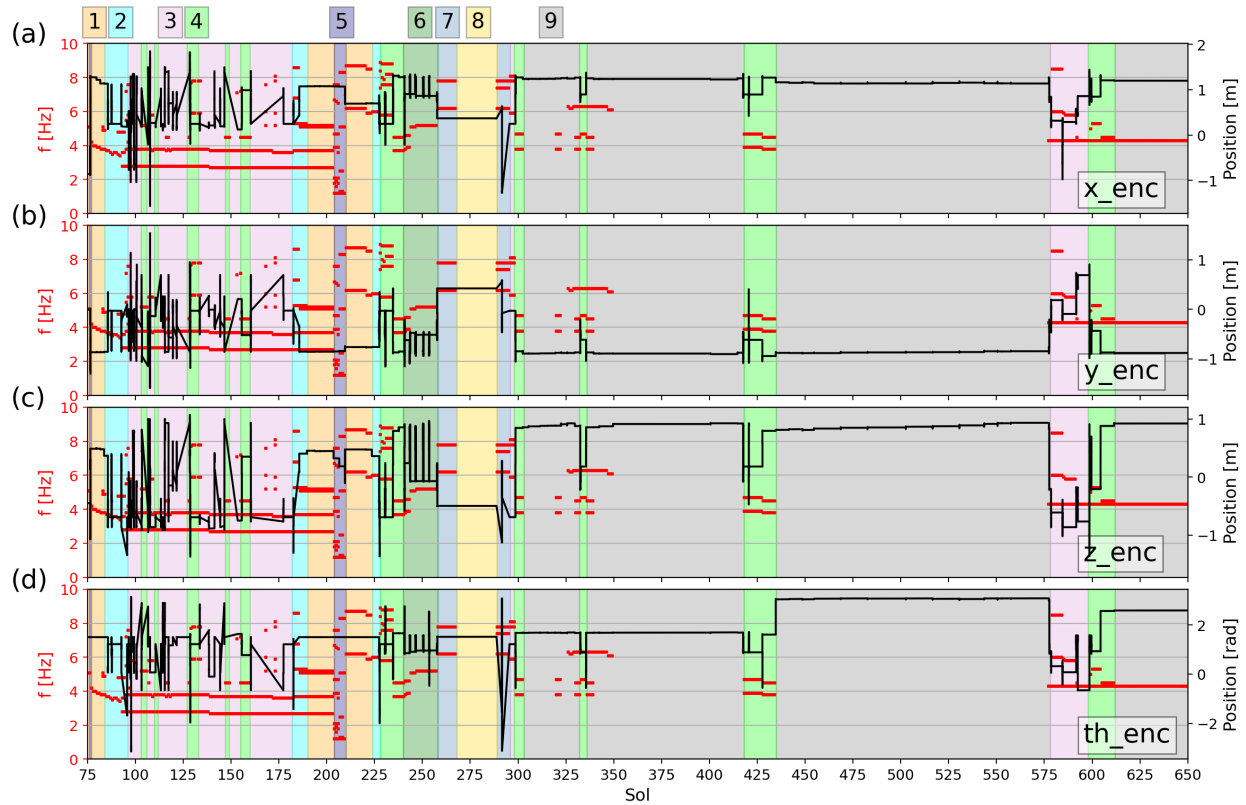


Figure 4. Summary of IDA position and temporary modes observed between Sols 75–650. Black lines denote the robotic arm position in the IDA reference frame (a) x , (b) y , (c) z , (d) th . ‘enc’ refers to encoder measurements. Slanted lines reflect long gaps without the arm position information. The red lines indicate the identified temporary modes. The background color gives the general IDA occupation: 1) Grapple holding HP³ housing, 2) Above HP³ - grapple out, 3) Over lander deck or miscellaneous positions, 4) Above HP³ - grapple secured, 5) Lifting HP³ housing, 6) Digging, 7) Next to western lander leg (parking position), 8) Solar conjunction, 9) Pinning the heat flow probe. The exact time intervals are given in Table 1.

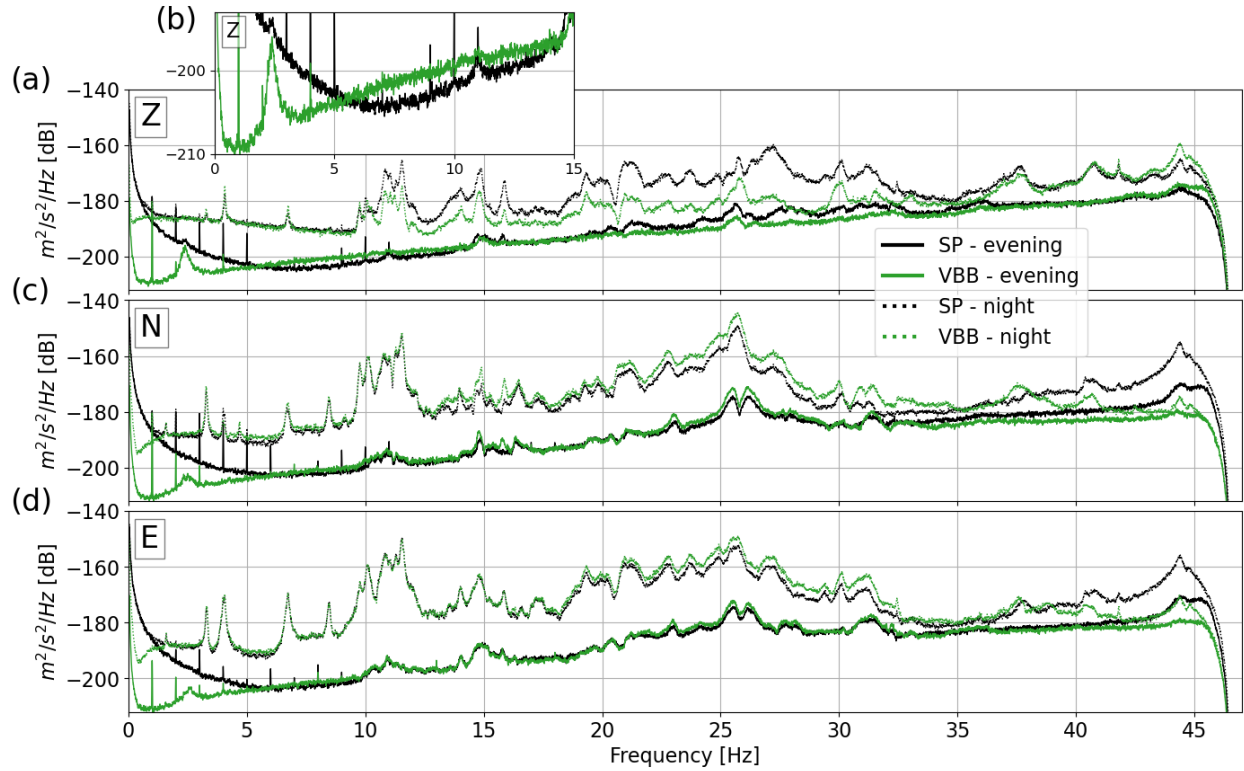


Figure 5. Comparison of VBB and SP seismometers. Spectra from Sol 422 for the (a) vertical (with inset (b) focusing on the frequency range from 0–15 Hz at lowest amplitudes), (c) north and (d) east components, computed with 120 s windows and 50% overlap. Data are taken from the night period 3:30–5:30 LMST (a period with steady but light winds) and the evening period 20:30–22:30 LMST (quietest period of the day).

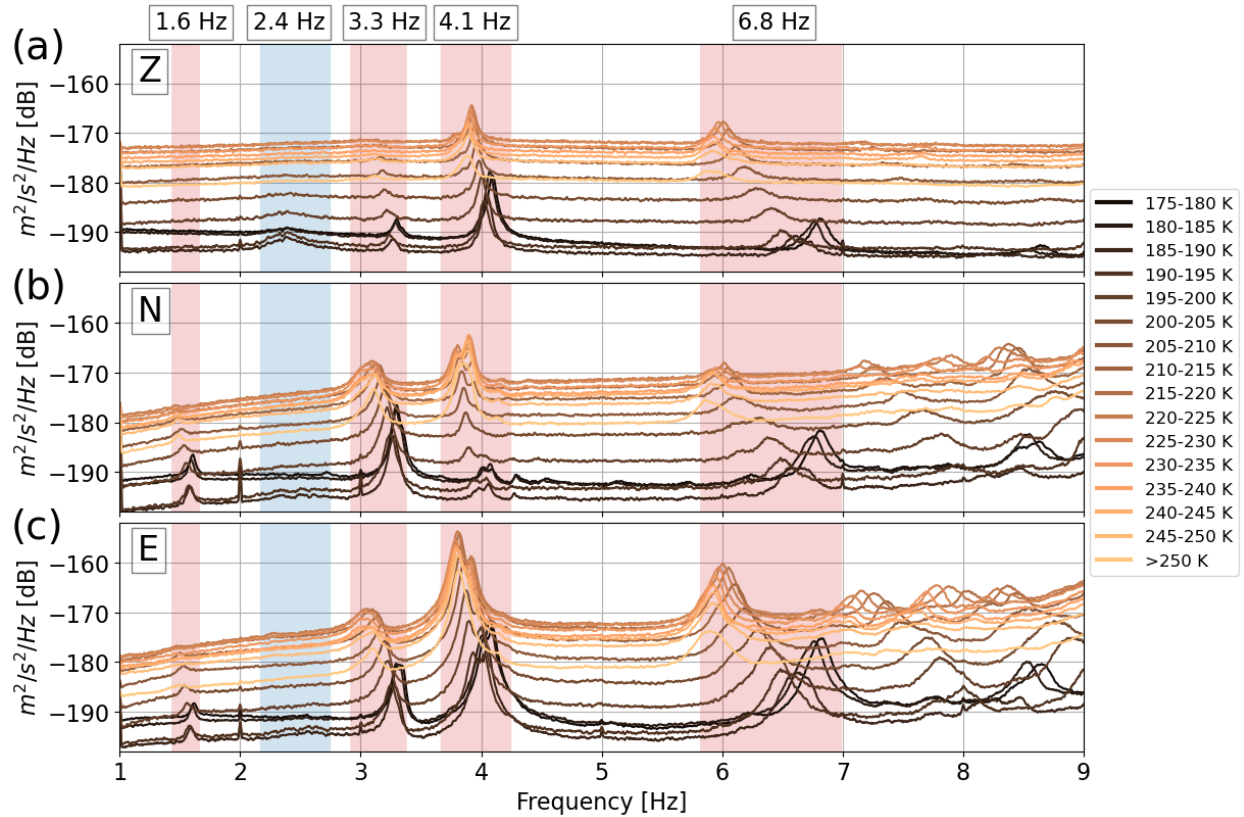


Figure 6. Frequency variation of modes with temperature. Averaged spectra by atmospheric temperature (sensor 2) on VBB (a) vertical, (b) north and (c) east component, computed with 120 s windows and 50% overlap. Each line corresponds to an average over 130 h, randomly selected from Sol 182–500. Highlighted are the frequency ranges of the 2.4 Hz (blue) and 1.6 Hz, 3.3 Hz, 4.1 Hz and 6.8 Hz modes (red).

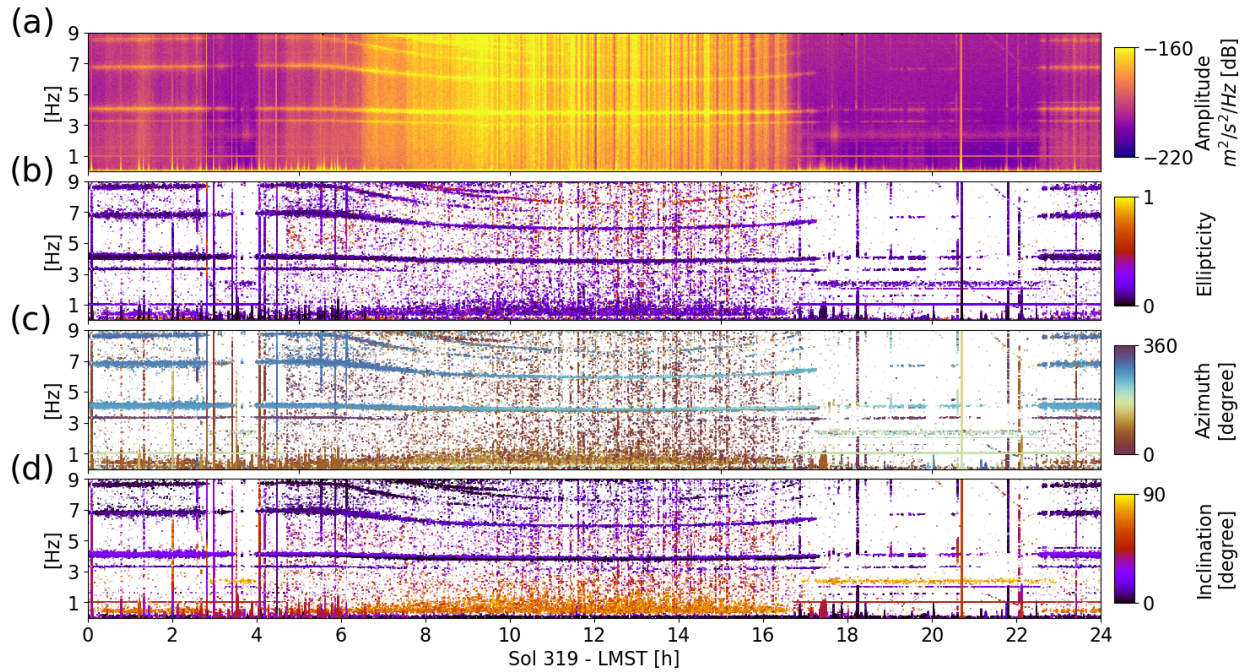


Figure 7. Polarization analysis Sol 319, VBB. (a) Three-component scalogram, (b) ellipticity, (c) major azimuth, and (d) major inclination, shown up to 9 Hz, computed with 120 s window length. The degree of polarization filter applied in (b)-(d) (with 120s window length, 0.05 Hz spectral width) removes all signals with degree of polarization values below 0.4.

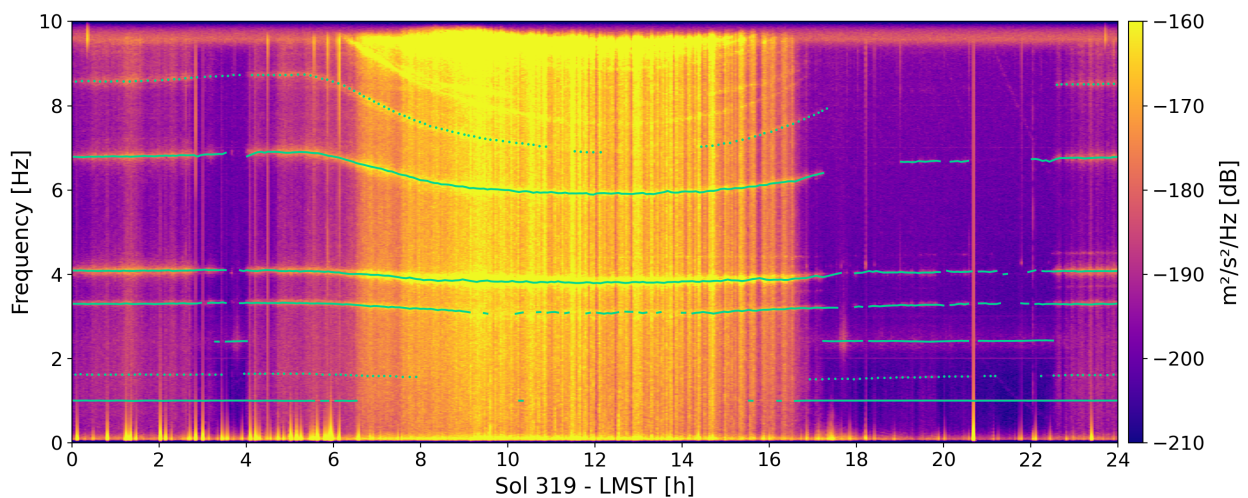


Figure 8. Tracking spectral peaks on Sol 319. The background shows the three-component scalogram from the 20sps VBB sensor, with 300s window length and 50% overlap. Solid green lines: automatically picked modes and tick noise, dotted green lines: manually picked modes.

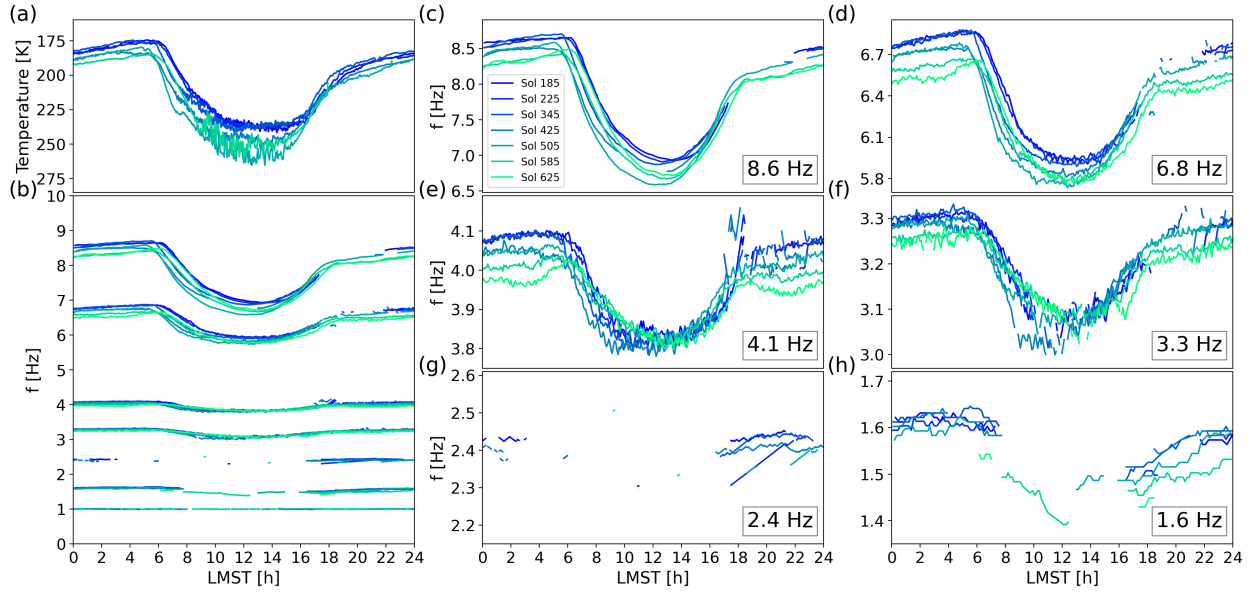


Figure 9. (a) Diurnal changes of atmospheric temperature measured by sensor 1 for different sols spread across the mission, from Sol 185 to Sol 625. (b)-(h) Diurnal changes in the natural frequency of modes for the same sols. (b) presents all modes plus the 1 Hz tick noise in a single figure, from 0–10 Hz. (c)-(h) show each mode in more detail. Depicted are both the automatically tracked signals (2.4 Hz (g), 3.3 Hz (f), 4.1 Hz (e), 6.8 Hz (d)) and the manually tracked modes (1.6 Hz (h), 8.6 Hz (c)). Note the inverse y-axis for (a).

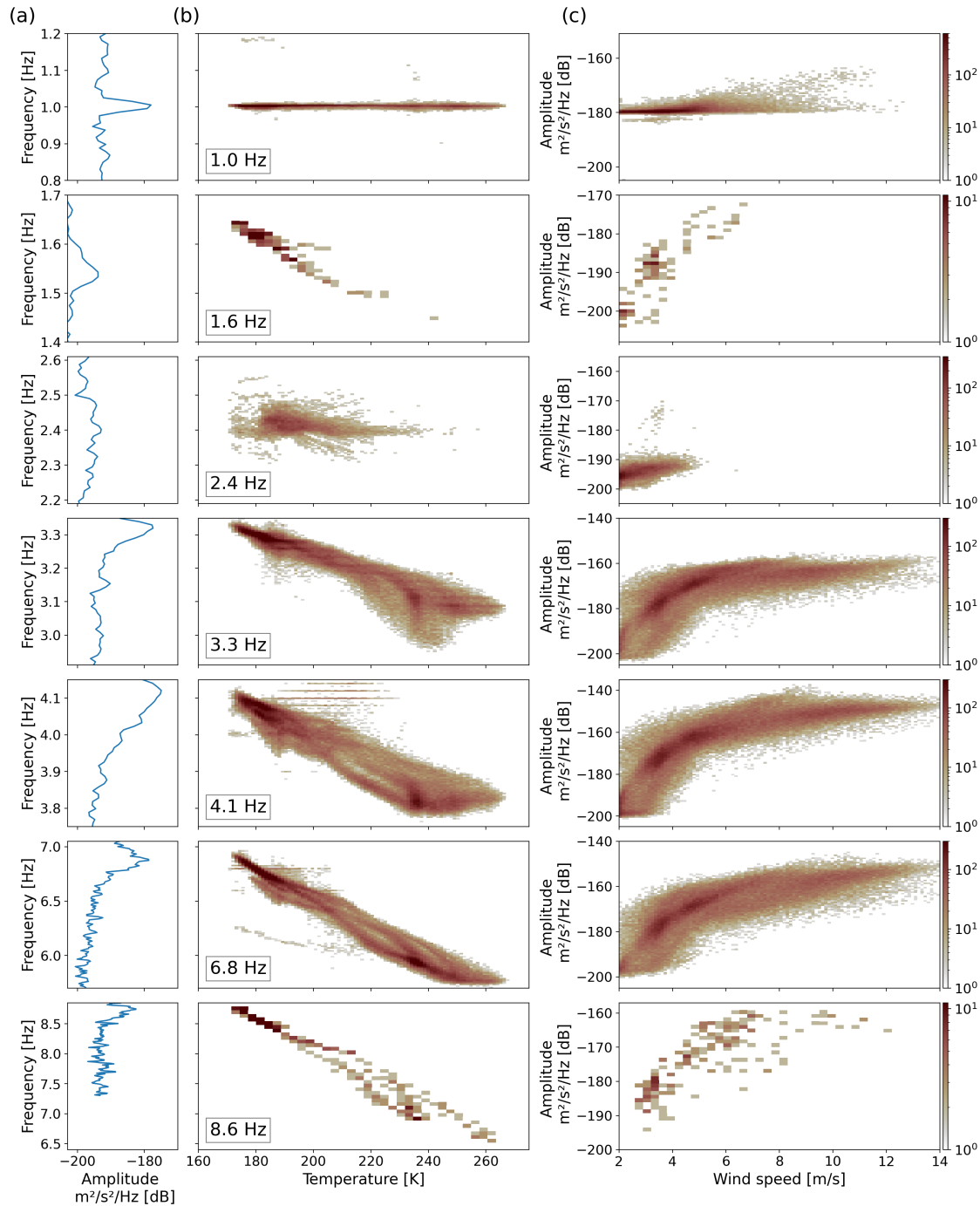


Figure 10. Variations of tracked spectral peaks across the entire mission. (a) Spectral peaks from the three-component scalogram at representative times individually selected where the peaks are clearly observed. Histograms of (b) the peak frequency against atmospheric temperature and (c) spectral amplitude against wind over the mission (Sol 182–649, where available). Depicted are the 1 Hz tick noise, and 1.6 Hz, 2.4 Hz, 3.3 Hz, 4.1 Hz, 6.8 Hz, and 8.6 Hz modes. Temperature sensor 1, and wind composite data are used. Note the different y-axes and log color scales between modes.

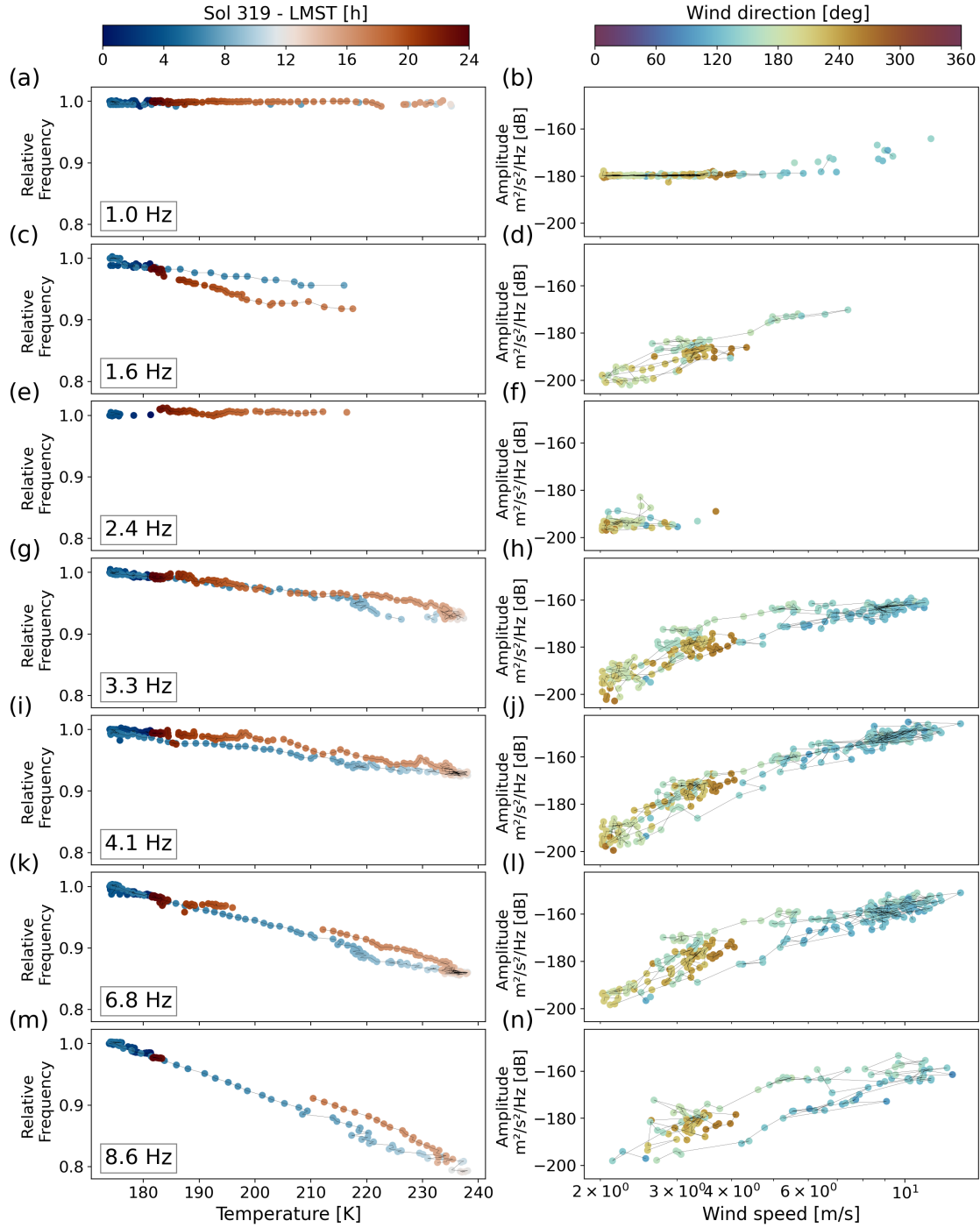


Figure 11. Variations of tracked spectral peaks across Sol 319. (left) Relative frequency (normalized with respect to frequency at 170 K) against atmospheric temperature and (right) amplitude against wind for all tracked peaks. (a,b) 1 Hz tick noise, (c,d) 1.6 Hz, (e,f) 2.4 Hz, (g,h) 3.3 Hz, (i,j) 4.1 Hz, (k,l) 6.8 Hz, and (m,n) 8.6 Hz modes. Colors on the left indicate time of day, colors on the right give the wind direction. Note the logarithmic x-axis on the right.

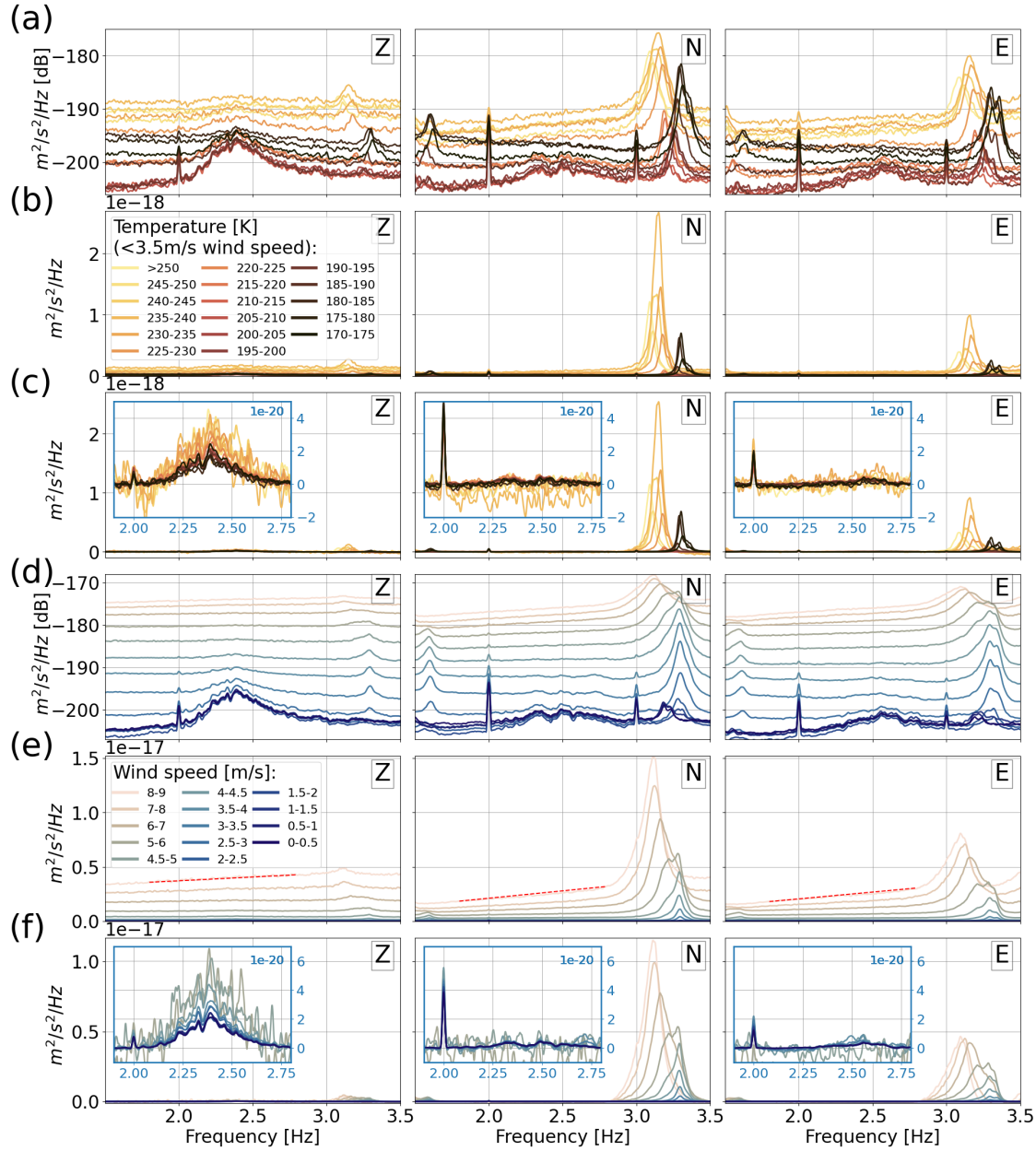


Figure 12. Overview of the VBB sensitivity to temperature (a)-(c) and wind (d)-(f), with focus on the 2.4 Hz resonance and 3.3 Hz lander mode. (a)-(c) show lines of average velocity spectra for each component of VBB binned by similar atmospheric temperatures (using sensor 1) on (a) logarithmic, (b) linear, and (c) linear scale with broadband noise baseline removed. The inset in (c) focuses on the 2.4 Hz resonance. Each binned line represents approx. 38 h of data with similar temperatures collected between Sols 182-650. (d)-(f) presents a similar analysis for wind speed. (d) is on a logarithmic scale, (e) linear scale, and (f) linear scale with baseline of broadband noise removed. The inset in (f) focuses on the 2.4 Hz resonance though only includes wind speeds up to 6 m/s. Each line represents between 118 h (low wind speeds) and 350 h (high wind speeds) of data, collected between Sol 182-500. Spectra are computed with 120 s window length. For the baseline, a linear fit of the average power values between 1.75-1.85 Hz to 2.75-2.85 Hz is removed for each binned spectrum. This line is indicated in (e), for the highest wind speed only.

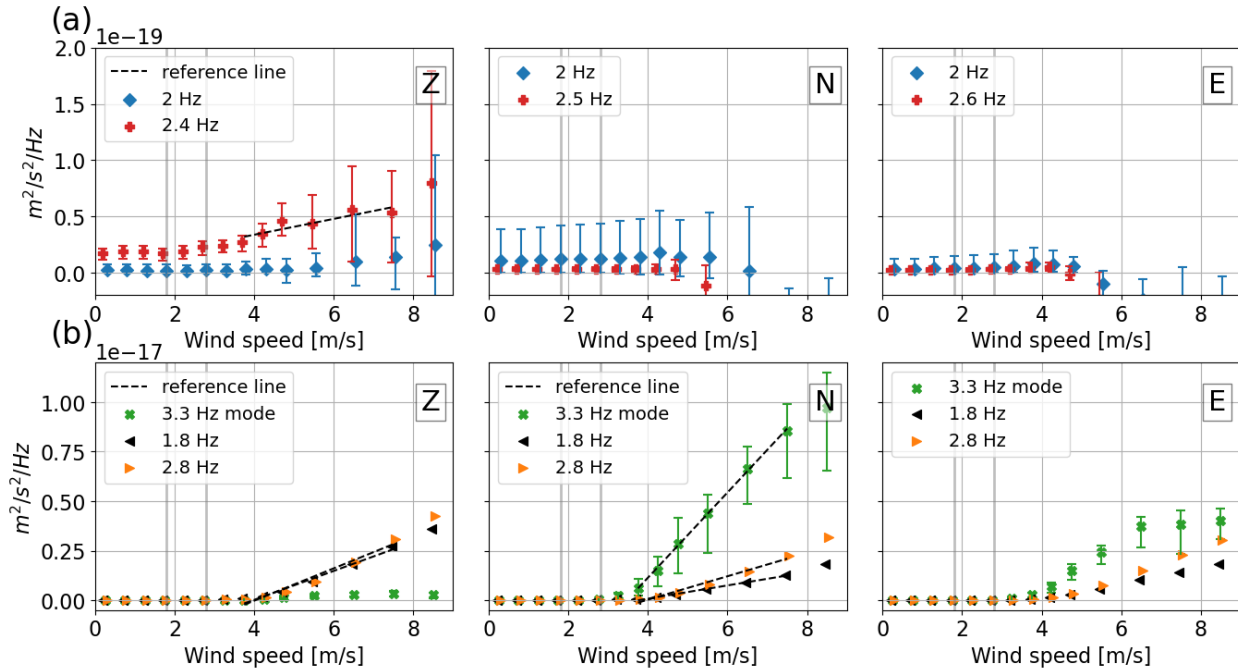


Figure 13. Correlation of the VBB amplitudes from the 2.4 Hz resonance (a) and 3.3 Hz lander mode (b) with wind speed. At each frequency and VBB component, we plot the excess power in velocity for each wind speed, extracted from Figure 12 (f) (these values include the baseline removal of the noise by subtracting a linear fit between averages of 1.75-1.85 and 2.75-2.85 Hz). (a) shows the excess power of the 2.4 Hz resonance and 2 Hz tick noise overtone in different wind conditions. (b) shows the excess power of the 3.3 Hz lander mode and increase of broadband noise level, using 1.8 Hz and 2.8 Hz as a proxy. A linear reference line between 3.75-7.5 m/s (black-dotted line) is given for the vertical component in (a), and the 3.3 Hz lander mode for the north component in (b), and additionally, for the broadband noise at 1.8 Hz and 2.8 Hz. The markers are slightly offset on the x-axis to avoid overlaps; the vertical gray lines mark wind measurements of 1.8 and 2.8 m/s, speeds below these levels are considered unreliable. The values represent the average excess power in a 0.1 Hz frequency bin around 2.4 Hz (Z), 2.5 Hz (N) and 2.6 Hz (E); and a 0.1 Hz bin around the varying peak of the 3.3 Hz mode. Additionally, we use a 0.05 Hz bin around 2 Hz, and 0.1 Hz bin around both 1.8 Hz and 2.8 Hz. The uncertainties are indicated by the min./max. values in these frequency ranges.

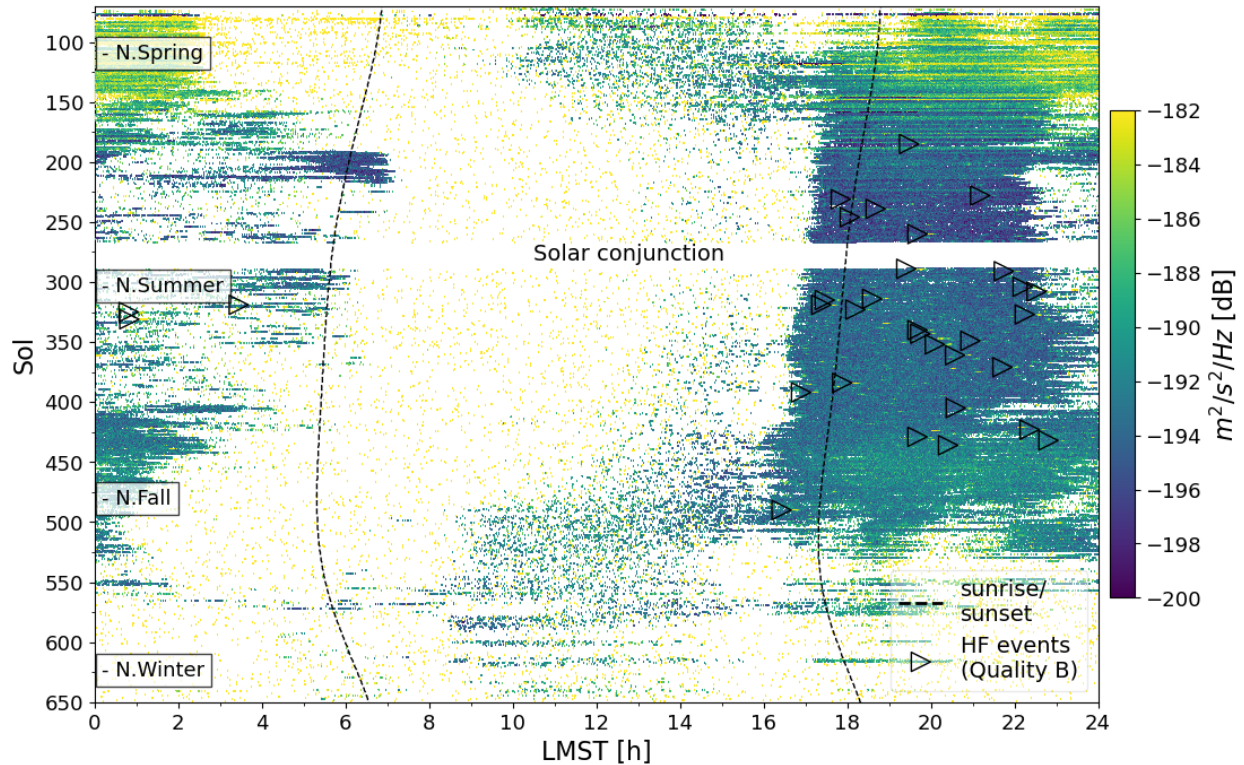


Figure 14. Seasonal variations in amplitude of VBB 2.4 Hz resonance. Shown is the vertical component (channels 58.BZC, 02/03.BHZ, see Data and Resources), extracted from a frequency band around 2.3–2.5 Hz, for the period Sol 70–650. Only periods when the amplitude in the 2.2–2.6 Hz band exceeds the broadband amplitude (1.2–3.0 Hz) by 6 dB are indicated. The energy onset times of 32 high quality, *high frequency* (HF) events with strong 2.4 Hz excitation are marked (see Data and Resources). The start of the seasons on the northern (N.) hemisphere, where InSight is located, are also indicated. Note no data are available during the solar conjunction.

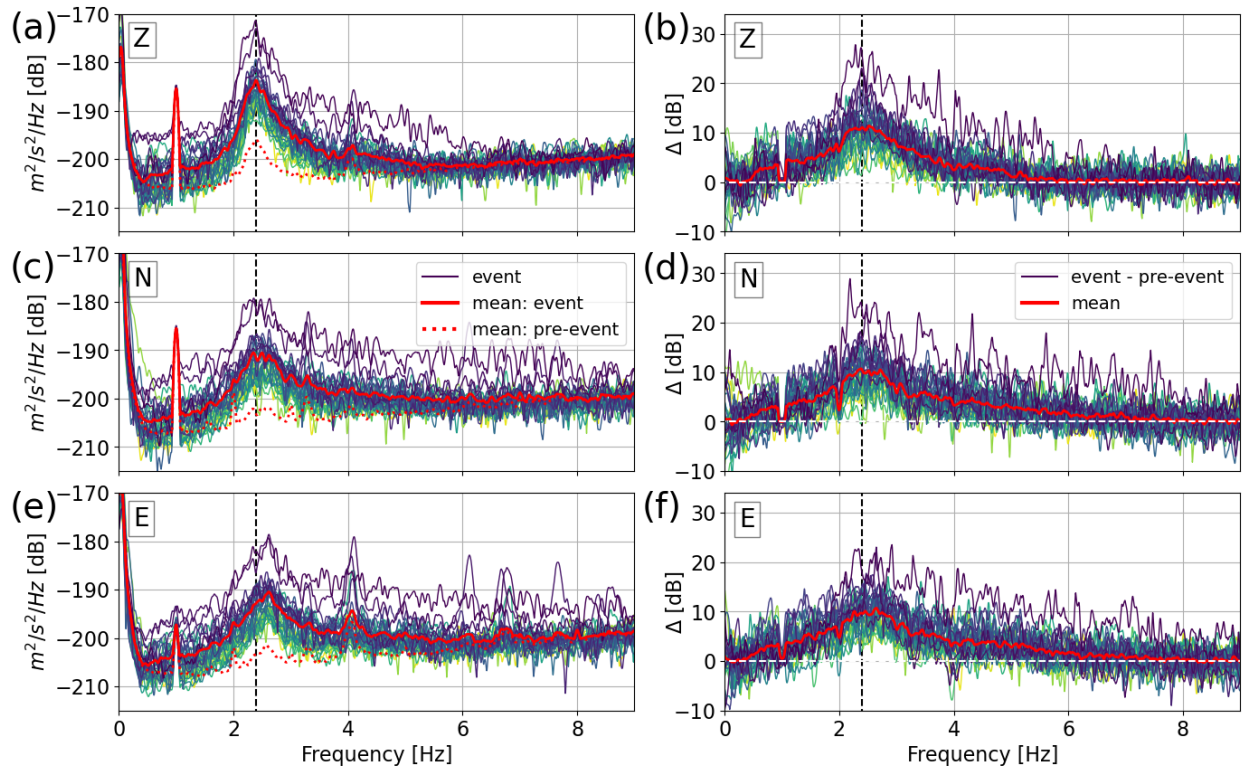


Figure 15. Overview of the excitation of the 2.4 Hz resonance during 32 *high frequency* events. The velocity spectra (30 s window length) are computed over the main S-wave energy for the (a) vertical, (c) north and (e) east components. The mean from all events (red) as well as from all pre-event time windows (red-dotted) are indicated. The spectral difference between each event and the pre-event signal is shown for the (b) vertical, (d) north and (f) east components. The vertical black-dotted line marks the 2.4 Hz frequency.

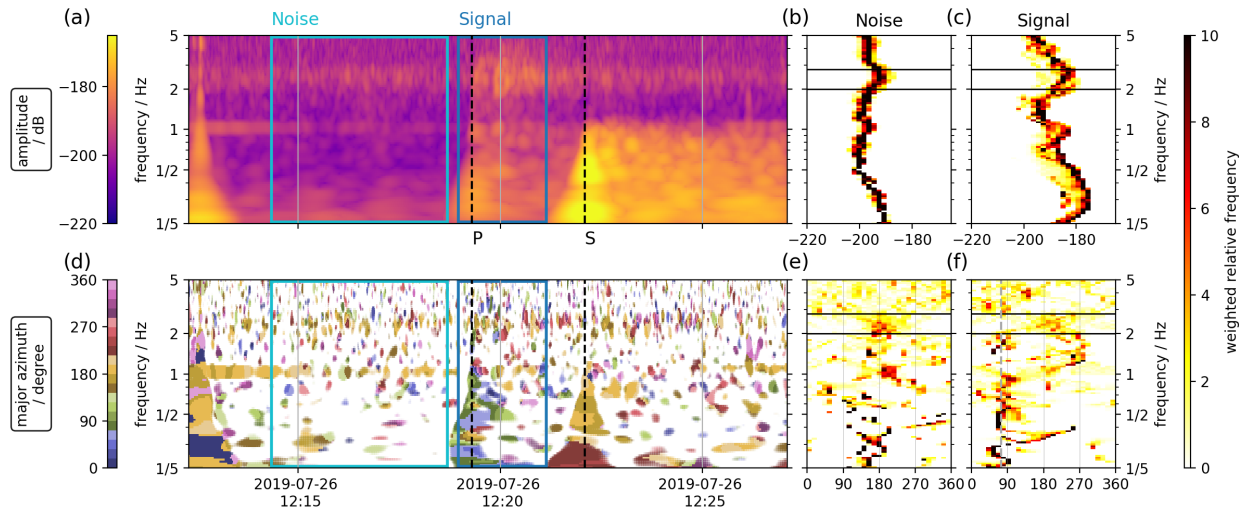


Figure 16. Polarization analysis for high quality, teleseismic event S0235b. (a) Three-component scalogram, and histograms of (b) a pre-event noise and (c) a signal time window. (d) Azimuth and (e), (f) respective histograms. We use the continuous wavelet transform and apply a degree of polarization filter that removes signals with degree of polarization values below 0.4. The signal window is taken as -20 to +110 s around the P arrival. Black horizontal lines in (b), (c), (e), and (f) mark the boundaries of the 2.4 Hz resonance. A dashed vertical line in (f) marks the MQS catalog back azimuth for the event.